Mitochondrial fission controls astrocyte morphogenesis and organization in the cortex

Maria Pia Rodriguez Salazar[1], Sprihaa Kolanukuduru[1,2], Valentina Ramirez[1,3], Boyu Lyu[4], Gracie Manigault[1], Gabrielle Sejourne[1], Hiromi Sesaki[5], Guoqiang Yu[6,7], Cagla Eroglu[1,8,9,10*]

1 The Department of Cell Biology, Duke University Medical Center, Durham, NC, USA

2 The Department of Psychology and Neuroscience, University of North Carolina at Chapel Hill, Chapel Hill, NC, USA

3 The Department of Psychology and Neuroscience, Duke University, Durham, NC, USA

4 Bradley Department of Electrical and Computer Engineering, Virginia Polytechnic Institute and State University, Arlington, VA, USA

5 Department of Cell Biology, John Hopkins University School of Medicine, Baltimore, MD

6 Department of Automation, Tsinghua University, Beijing 100084, China

7 IDG/McGovern Institute for Brain Research, Tsinghua University, Beijing 100084, China

8 Aligning Science Across Parkinson's (ASAP) Collaborative Research Network, Chevy Chase, MD

9 The Department of Neurobiology, Duke University Medical Center, Durham, NC, USA

10 Howard Hughes Medical Institute, Duke University Medical Center, Durham, NC, USA

*Corresponding author: Cagla Eroglu: cagla.eroglu@duke.edu

Summary:

During cortical astrocyte morphogenesis, mitochondria fragment and decrease in size to populate distal astrocyte processes. Drp1-mediated mitochondrial fission is necessary for peripheral astrocyte process formation. Astrocyte-specific Drp1 loss induces astrocyte reactivity, disrupts cortical astrocyte organization, and dysregulates PAP proteins including gap-junction protein Connexin 43 abundance.

ABSTRACT

Dysfunctional mitochondrial dynamics are a hallmark of devastating neurodevelopmental disorders such as childhood refractory epilepsy. However, the role of glial mitochondria in proper brain development is not well understood. We show that astrocyte mitochondria undergo extensive fission while populating astrocyte distal branches during postnatal cortical development. Loss of mitochondrial fission regulator, Dynamin-related protein 1 (Drp1), decreases mitochondrial localization to distal astrocyte processes, and this mitochondrial mislocalization reduces astrocyte morphological complexity. Functionally, astrocyte-specific conditional deletion of Drp1 induces astrocyte reactivity and disrupts astrocyte organization in the cortex. These morphological and organizational deficits are accompanied by loss of perisynaptic astrocyte process (PAP) proteins such as gap junction protein Connexin 43. These findings uncover a crucial role for mitochondrial fission in coordinating astrocytic morphogenesis and organization, revealing the regulation of astrocytic mitochondria dynamics as a critical step in neurodevelopment.

INTRODUCTION

Mitochondria are dynamic organelles that move, divide, and fuse in response to changing cellular states (Friedman and Nunnari, 2014; Youle and van der Bliek, 2012). Localized functions of mitochondria within cells are governed by fusion, fission, and trafficking processes, collectively referred to as mitochondrial dynamics (Ni et al., 2015). Mitochondrial dynamics are particularly important for the function and development of highly compartmentalized cells such as neurons, where mitochondria within distal compartments perform key functions including ion buffering, energy production, and local protein translation (Billups and Forsythe, 2002; López-Doménech and Kittler, 2023; Rangaraju et al., 2019). Furthermore, distal mitochondria regulate cellular morphology of neurons through focalized ATP generation for actin polymerization at growth cones, and disruptions in mitochondrial dynamics result in stunted neurite growth (Courchet et al., 2013; Smith and Gallo, 2018; Steketee et al., 2012). Indeed, mutations in the genes that control the mitochondrial dynamics' machinery cause severe neurodevelopmental disorders, such as forms of childhood refractory epilepsy (Abati et al., 2022; Vanstone et al., 2016).

Despite the clear importance of mitochondrial dynamics in brain development, the role of this organelle in non-neuronal brain cells is less well understood. In particular, astrocytes are the most abundant glial cells in the brain and have highly ramified processes that infiltrate the neuropil in the brain parenchyma (Verkhratsky et al., 2017) . These fine astrocyte processes interact with synapses, vasculature, and other glia (Allen and Lyons, 2018) where they regulate synapse formation, neurotransmitter and ion buffering, and maintain the blood-brain barrier (Alvarez et al., 2013; Chung et al., 2015). Intriguingly, astrocyte peripheral processes are loaded with mitochondria at higher densities than the surrounding neuropil (Lovatt et al., 2007), and their mitochondria are recruited to perisynapses in response to neuronal activity (Stephen et al., 2015), linking astrocyte mitochondrial dynamics and synapse function. Indeed, mature astrocyte mitochondria localize to functional microdomains in their arbors, where mitochondria regulate distal calcium dynamics to provide metabolic support in response to neuronal activity (Agarwal et al., 2017). Furthermore, recent work established that immature astrocytes have a high oxidative capacity and require mitochondrial biogenesis for proper morphogenesis and synapse formation (Zehnder et al., 2021). However, the role of mitochondrial dynamics in astrocyte development is unknown.

Beyond their morphological complexity, astrocytes further regulate brain homeostasis by tiling the entire brain parenchyma in evenly dispersed, non-overlapping domains. This organization enables astrocytes to form an extensive network that facilitates long-distance communication via gap junction-coupling between the distal processes of neighboring astrocytes (Bushong et al., 2002; Giaume et al., 2010). Tiling is absent in immature astrocytes, becomes established as astrocytes mature, and is regulated by the same machinery that ensures proper gap junction coupling (Baldwin et al., 2021). Cx43 is the most abundant gap junction protein in the brain and is almost exclusively expressed in astrocytes (Rash et al., 2001). Beyond its gap junction roles, Cx43 has cell-adhesion functions that drive astrocyte morphogenesis and migration (Kameritsch et al., 2012; Lagos-Cabré et al., 2019). Importantly, both tiling and gap junction-coupling are disrupted in many forms of brain injury and disease such as epilepsy and traumatic brain injury, indicating the importance of the proper establishment of astrocyte networks in brain homeostasis (Cheung et al., 2023; Clasadonte et al., 2017; Hösli et al., 2022; Oberheim et al., 2008).

Here, we investigated the role of mitochondrial dynamics in astrocyte morphogenesis, development, and function. We found that astrocyte mitochondria robustly increase in number and decrease in size to populate distal astrocyte processes during postnatal development, linking mitochondrial fission to astrocyte morphogenesis. Dynamin-related protein 1 (Drp1), encoded by the gene *Dnm1l,* is a highly conserved GTPase that controls mitochondrial fission (Smirnova et al., 2001). Upon mitochondrial division, Drp1is recruited to the outer mitochondrial membrane to perform GTP hydrolysis-driven scission (Smirnova et al., 2001). Complete loss of Drp1 is embryonically lethal in mice (Wakabayashi et al., 2009b) and mutations in human *DNM1L* are linked to aggressive forms of developmental delay and childhood refractory epilepsy (Fahrner et al., 2016; Liu et al., 2021). Despite the causal link between Drp1 function and proper brain development, the role of Drp1 in astrocyte morphogenesis and development is unknown.

RESULTS

Mitochondria increase in number and decrease in size during cortical astrocyte morphogenesis

In mature astrocytes, mitochondria occupy the entirety of the astrocyte arbor (Lovatt et al., 2007) and this mitochondrial dispersion is remodeled in response to injury or disease (Gollihue and Norris, 2020; Motori et al., 2013). However, how the mitochondrial network is established and modified in developing astrocytes is not well understood. How do mitochondrial transport, fission, or fusion dynamics orchestrate the distribution of astrocytic mitochondria during morphogenesis? To address this question, we first investigated how the mitochondrial network transforms during astrocyte maturation to populate the arbors. To do so, we used Postnatal Astrocyte Labeling by Electroporation (PALE) (Stogsdill et al., 2017) to fluorescently label sparse populations of astrocytes in the developing mouse V1 visual cortex. We used Mito-EGFP floxed mice (Agarwal et al., 2017), in which EGFP is targeted to the inner mitochondrial membrane protein cytochrome c oxidase, to label all mitochondria in Cre-expressing cells. We electroporated two plasmids into the ventricles of P0 mice— a pCAG-Cre plasmid to turn on the mitochondrial GFP and an mCherry-CAAX plasmid to label astrocyte membranes. Then using confocal microscopy, we imaged and analyzed astrocytes from layers 2/3, 4, and 5 of the developing visual cortex. This approach allowed us to visualize and quantify astrocyte morphology and their mitochondrial content throughout postnatal cortical development using confocal microscopy and morphometric analyses (Fig. 1A).

We focused our studies on the first 3 weeks of postnatal astrocyte development (P4, P7, P14, P21, Fig. 1B), because cortical astrocytes become morphological mature during this period (Clavreul et al., 2019; Stogsdill et al., 2017). As expected, astrocytes undergo robust growth and elaboration, increasing their overall cell volume approximately 20-fold between P4 and P21 (Fig. 1C). Concurrently, we found that total astrocyte mitochondrial volume per cell increased 5-fold between P4 and P14 and then remained constant between P14 and P21 (Fig. 1D). We next quantified total mitochondrial volume per cell normalized to astrocyte cell volume, hereafter referred to as total mitochondrial occupancy. We found total mitochondrial occupancy decreased during development due to the robust increase in astrocyte cell volume (Fig. 1E). Importantly, astrocyte mitochondria increased in number and decreased in size on average during these first two postnatal weeks (Fig.

1F-G), indicating mitochondria division (fission) occurs concurrently with astrocyte morphogenesis.

Mitochondria occupy fine astrocyte processes concurrently with morphogenesis *in vitro*

The recruitment of mitochondria to the distal edge of developing cell processes in other compartmentalized cells is required for cytoskeletal remodeling and branch outgrowth (Cunniff et al., 2016; Smith and Gallo, 2018). However, the spatiotemporal distribution of mitochondria during astrocyte arborization and whether astrocyte mitochondria are present at the tips of their developing peripheral processes is not known. The highly complex morphology of astrocytes *in vivo* obstructs our ability to track and analyze individual astrocyte processes and their mitochondria. Therefore, we investigated how mitochondria are distributed throughout the astrocyte arbor during morphological growth using an *in vitro* astrocyte-neuron co-culture system. Astrocytes cultured on top of neurons gain a complex morphology compared to astrocytes cultured alone or with non-neuronal cells (Stogsdill et al., 2017). Thus, we used astrocyte-neuron co-cultures to stimulate astrocyte ramification and track how mitochondrial number, size, and distribution change during process elaboration. We isolated and transfected primary cortical rat astrocytes with cytosolic GFP and MitoDsRed constructs to label astrocytes and their mitochondria, respectively. Transfected astrocytes were then plated onto rat cortical neuron monolayers for 4, 12, 24, and 48 hours (Fig. 2A-B).

We developed a Matlab-based image analysis program, Seg_Astro (https://github.com/Eroglu-Lab/seg_cul_astro_app/tree/main) to quantify branch number, mitochondrial number, and mitochondrial size across astrocyte arbors. Seg_Astro uses branch width and branchpoints to determine the astrocyte branch hierarchy and assign four branch types: 1) soma and primary processes, 2) secondary processes, 3) fine processes, and 4) the terminal tips of processes (Fig. 2C). Seg_Astro then bins mitochondria into these 4 types of branches and outputs branch number, mitochondrial number, and mitochondrial size per branch type. We excluded mitochondrial measurements from the soma and primary branches of astrocytes as mitochondria form dense network in these compartments that cannot be distinguished as discrete mitochondria for number and size quantification.

153 Seg_astro quantification showed a significant increase across all astrocyte branch types (primary,
154 secondary, fine, and terminal) between 4hr and 48hr in culture. Strikingly, astrocyte fine branches
155 had the largest increase in number, ~5-fold from 4 to 48 hours in culture (Fig 2D). Intriguingly,
156 mitochondria were present across all astrocyte branch types including fine and terminal, as early
157 as 4 hours and through 48 hours in co-culture (Fig. 2B Inset and 2E). These results show that
158 mitochondria occupy distal processes during astrocyte branch development in vitro and suggest
159 that mitochondrial recruitment to these distal processes may be required for sustained growth of
160 astrocyte arbors.

161 Our analyses also revealed astrocyte mitochondria numbers increased across all branch types
162 throughout time in culture, with fine branches housing the largest increase in number of
163 mitochondria from 4 to 48hrs in culture compared to other branch types (secondary and terminal)
164 (Fig. 2E). This unique fine branch mitochondrial number increase correlates with the high increase
165 in fine branch numbers (both ~5-fold) compared to all other branch types (Fig. 2D), indicating that
166 the robust increase in astrocyte fine branch number during astrocyte morphogenesis is linearly
167 scaled with increased occupancy of proportionally high mitochondrial numbers. While
168 mitochondrial numbers increased, average mitochondrial size decreased across all astrocyte branch
169 types throughout time in culture *except* in fine processes, which housed consistently small
170 mitochondria throughout morphogenesis (Fig. 2F). This result suggested that mitochondrial fission
171 may be required for mitochondrial recruitment to the growing fine/distal processes as there may
172 be a maximum size threshold for mitochondria to occupy fine astrocyte branches. These data echo
173 and expand upon our *in vivo* findings and implicate a role for mitochondrial division in distal
174 astrocyte process morphogenesis.

175

176 **Drp1-induced mitochondrial fission is required for distal astrocyte process formation and**
177 **mitochondrial localization *in vitro***

178 Because cortical astrocyte morphogenesis occurred concurrently with extensive mitochondrial
179 fragmentation *in vivo* and *in vitro*, we next investigated the role of mitochondrial fission in
180 astrocyte development. We knocked down Drp1, the key GTPase regulator of mitochondrial
181 fission (Smirnova et al., 2001) (Fig. 3A-C), in astrocytes using a small hairpin RNA (shRNA)
182 targeting both the rat and mouse mRNAs (Sup. Fig. 2A-B) and assessed how it affected astrocyte

183 morphological complexity in co-culture with neurons. We co-transfected GFP-expressing shDrp1
184 or a scrambled control shRNA (shControl) and MitoDsRed into astrocytes and co-cultured them
185 on neurons for 48 hours (Fig. 3C). shDrp1 astrocytes displayed robustly hyperfused and elongated
186 mitochondria as we would expect when inhibiting mitochondrial fission (Fig. 3C). We used
187 Seg_Astro to quantify mitochondrial and branch number per branch type in shControl and shDrp1
188 astrocytes (Fig. 3D). We found that Drp1 knockdown significantly decreased mitochondria
189 numbers in all branch types measured- secondary, fine, and terminal astrocyte processes compared
190 to control. The largest decrease in mitochondria numbers was in fine/distal branches, to less than
191 40% of shControl (Fig. 3E). Interestingly, shDrp1 astrocytes only had a significant loss of fine and
192 terminal branch numbers compared to shControl, with the greatest decrease quantified in fine
193 branch numbers (~40% of control, Fig. 2F). Therefore, both fine branch number and fine branch
194 mitochondria number in shDrp1 astrocytes decreased to the same degree compared to control (Fig.
195 2E-F). Drp1 loss did not affect primary or secondary branch numbers, despite secondary branches
196 also displaying a significant decrease in mitochondrial numbers in shDrp1 conditions (Fig. 3F).
197 These data demonstrate that Drp1 is specifically required for fine and distal astrocyte process
198 formation, likely through regulation mitochondrial size and recruitment to these fine processes.

199 To determine if Drp1 GTPase activity-driven scission is necessary for its role in astrocyte distal
200 process morphogenesis, we implemented human Drp1 constructs that are resistant to shDrp1 (Sup.
201 Fig. 2A); wild-type human Drp1 (hDrp1) and GTPase-dead point mutant human Drp1 (hDrp1-
202 K38E) (Fig. 3B) (König et al., 2021). The co-transfection of shDrp1 with hDrp1 rescued astrocyte
203 distal process formation compared to shDrp1 alone, whereas the GTPase-dead counterpart could
204 not (Fig. 3G-K). Together these data reveal that Drp1-mediated mitochondrial fission is necessary
205 for the formation of fine/distal astrocyte branches *in vitro*. These data also suggest that
206 mitochondrial recruitment to distal processes is facilitated by mitochondrial fission, and this
207 recruitment is required for astrocyte fine branch formation and/or stabilization during astrocyte
208 morphological growth.

209

210 **Drp1 controls mitochondrial occupancy and distal astrocyte process morphogenesis *in vivo***

211 Because Drp1 is required for distal astrocyte branch formation *in vitro,* we next tested whether
212 Drp1-mediated mitochondrial fission (Fig. 4A) would play a similar role in cortical astrocyte

213 morphogenesis *in vivo.* To address this question, we used PALE to electroporate plasmids with
214 shDrp1 or shControl into the ventricle of P0 Mito-EGFP floxed mice. These plasmids also express
215 a membrane-tagged mCherry reporter, which we used to quantify astrocyte morphology. They
216 were delivered together with a Cre-expressing plasmid, which drives Mito-EGFP expression to
217 determine mitochondrial morphology at P21. We used Imaris to render 3D surfaces of astrocytes
218 and their mitochondria and measure overall astrocyte territory size, the volume of distal neuropil-
219 infiltrating astrocyte processes (Neuropil Infiltration Volume; NIV), and total mitochondrial
220 volume, size, and number in the whole astrocyte or the distal processes. Using these methods, we
221 investigated how loss of Drp1 in cortical astrocytes *in vivo* impacted astrocyte territory size, distal
222 process formation, and mitochondrial localization within the astrocyte arbors.

223 Importantly, Drp1 knock-down robustly modified astrocyte mitochondria, significantly increasing
224 average mitochondrial size and decreasing mitochondrial number compared to shControl
225 astrocytes (Sup. Fig. 2A-B). These data validated Drp1 loss inhibited mitochondrial fission in
226 astrocytes, resulting in longer and fewer mitochondria *in vivo,* as we had observed *in vitro* (Fig.
227 3C). Interestingly, shDrp1 had no effect on astrocyte territory size (Fig. 4B), which is determined
228 by larger astrocyte process outgrowth. However, Drp1 knockdown significantly decreased
229 mitochondrial localization to distal astrocyte regions, which was accompanied by a significant
230 decrease in the volume of distal neuropil-infiltrating astrocyte processes (Fig. 4C-D). These results
231 suggest that mitochondrial fission controls mitochondrial recruitment to distal/perisynaptic
232 astrocyte processes which is required for proper neuropil infiltration by astrocytes *in vivo*.

233 To determine if distal astrocyte process formation was specifically controlled by Drp1-induced
234 mitochondrial fission or a byproduct of modifying mitochondrial dynamics in general, we tested
235 how disrupting mitochondrial fusion by knocking down Mitofusin1 or inhibiting mitochondrial
236 transport by knocking down Miro1, modified astrocyte morphogenesis and mitochondrial
237 occupancy. Mitofusin1 (Mfn1) is a GTPase on the outer membrane of mitochondria that facilitates
238 fusion (Chen et al., 2003) (Fig. 4E). Miro1 is a GTPase adaptor that tethers the outer mitochondrial
239 membrane to cytoskeletal motors for mitochondrial transport (Fransson et al., 2006) (Fig. 4I). We
240 used PALE to electroporate shMfn1 or shMiro1 constructs (Sup. Fig. 1C-E). First, we found that
241 Mfn1 knock-down in astrocytes significantly increased mitochondrial number and decreased
242 average mitochondrial size compared to shControl, indicating inhibited mitochondrial fusion in
243 shMfn1 astrocytes (Sup. Fig. 2A, C). shMiro1 had no effect on astrocyte mitochondrial numbers

244 but had a slight yet significant increase in mitochondrial size (Sup. Fig. 2A, D). Interestingly,
245 silencing Mfn1 caused a reduction in astrocyte territory size (Fig. 4F) but did not alter the volume
246 of distal neuropil-infiltrating processes (Fig. 4G-H), indicating mitochondrial fusion may play a
247 role in astrocyte territory outgrowth independently of distal process complexity. Despite increased
248 mitochondrial numbers, significantly decreased mitochondrial size in Mfn1 KD astrocytes may
249 stunt astrocyte territory outgrowth. Miro1 knockdown did not impact astrocyte morphology (Fig.
250 4J-K) but caused an increase in the volume of mitochondria localized at the distal astrocyte
251 processes (Fig. 4L), suggesting Miro1-mediated mitochondrial trafficking may regulate retrograde
252 mitochondrial transport in developing astrocytes. Lastly, total mitochondrial content (total
253 mitochondrial volume normalized to total cell volume) was not altered in any of the genetic
254 manipulations of mitochondrial dynamics (Sup. Fig. 2 E-H). This result indicates that
255 dysfunctional mitochondrial fission, fusion, or transport impacts astrocyte morphogenesis
256 proportionally to changes in the mitochondrial network. Taken together, we found that
257 mitochondrial dynamics are key regulators of astrocyte morphology, likely through the control of
258 mitochondrial localization to nascent processes. Our findings show that astrocyte territory growth
259 (large primary/secondary processes) does not require Drp1 function. However, Drp1-induced
260 mitochondrial fission, but not mitochondrial fusion or transport, is necessary for the formation of
261 distal neuropil-infiltrating astrocyte processes *in vivo.*

262

263 **Drp1 is required for astrocyte organization during postnatal cortical development**

264 During our PALE studies investigating the role of Drp1 in cortical astrocyte morphogenesis, we
265 observed an unusual clustering phenotype in shDrp1-transfected astrocytes compared to shControl
266 at P21 (Fig. 5A). PALE time course experiments from P7-P21 revealed that shDrp1 astrocytes
267 clustered as early as P7, and the clustering effect was cumulative across timepoints, reaching a
268 nearly 4-fold increase in cluster area compared to control by P21 (Fig. 5B). To determine if this
269 phenotype was due to a prolonged or exuberant astrocyte proliferation, we used Click-IT EdU
270 chemistry to label proliferating cells in the cortex of PALE mice. shControl and shDrp1 plasmids
271 were electroporated at P0, then EdU was injected intraperitoneally every two days from P3 to P13
272 and brains were collected 15 hours after EdU injection from P4 through P14 (Sup Fig. 3A). We
273 did not find any evidence of increased or prolonged cell proliferation in shDrp1 transfected

274 astrocytes compared to control (Sup. Fig. 3B, C), indicating astrocyte clustering in shDrp1-
275 transfected astrocytes is not caused by over proliferation. These shDrp1 astrocyte clusters
276 remained into adulthood (in 2 and 6-month-old mice, Sup. Fig. 3D, E), demonstrating astrocyte
277 clustering due to Drp1 loss is not a transient developmental phenomenon that resolves after
278 maturation.

279 Cortical astrocytes organize themselves into a network of evenly dispersed, non-overlapping
280 domains, which is critical for proper brain function (Bushong et al., 2004). Because early postnatal
281 loss of Drp1 led to cortical astrocyte clustering, we next sought to understand whether these
282 astrocyte clusters displayed disrupted astrocyte organization. To do so, we measured the nearest
283 neighbor distance between Sox9+ astrocyte nuclei to investigate whether shDrp1 astrocyte clusters
284 consisted of adjacent astrocytes that maintained their evenly dispersed astrocyte organization
285 (equidistant nuclei), or disorganized astrocytes with inconsistent nuclei distances (Fig. 5C). First,
286 we found that Drp1 knockdown clusters contained ~4 nuclei on average compared to control
287 astrocytes which only contain 1 nucleus (Fig. 5D), confirming that shDrp1-transfected astrocyte
288 clusters comprised multiple astrocytes. Importantly, shDrp1 astrocyte clusters had a 3-fold
289 decrease in nearest neighbor distance compared to control astrocytes (Fig. 5E), indicating a
290 disorganization among cortical astrocytes when Drp1 is knocked down. These data show that loss
291 of Drp1 impairs the astrocyte organization in the cortex by inducing clustering, suggesting Drp1
292 may play a role in the establishment of astrocyte tiling during development. Taken together these
293 data demonstrate that Drp1-induced mitochondrial fission promotes both astrocyte morphogenesis
294 and organization during postnatal development in the mouse cortex.

295 Astrocyte organization in the cortex is mechanistically linked to the formation of a gap junction-
296 coupled astrocyte network (Baldwin et al., 2021). In particular, proper expression and localization
297 of Connexin 43 (Cx43) , the most abundant astrocytic gap junction protein (Dermietzel et al.,
298 1991), is required for the establishment of non-overlapping astrocyte territories (Baldwin et al.,
299 2021; Lagos-Cabré et al., 2019). Furthermore, Cx43 has non-gap junction functions such as cell
300 migration and cell-cell interactions, which control astrocyte migration and localization in the
301 cortex (Homkajorn et al., 2010). Because we observed astrocyte disorganization and clustering in
302 PALE shDrp1 astrocytes, we next wondered if loss of Drp1 caused concurrent disruptions of gap
303 junctions. To test this possibility, we quantified Cx43 via immunohistochemistry within shDrp1
304 and shControl PALE astrocytes. Strikingly, shDrp1 astrocyte clusters had a 5-fold decrease in

305 Cx43 with visible "holes" of Cx43 staining coinciding with the shDrp1 astrocyte clusters (Fig. 5F-
306 G). Interestingly, Cx43 levels in shDrp1 astrocytes that were not part of shDrp1 astrocyte clusters
307 or on the periphery of these clusters also exhibited significantly decreased Cx43 protein levels
308 (Fig. 5F-G), suggesting that inhibited mitochondrial fission leads to decreases of Cx43 protein in
309 both single and clustered shDrp1 astrocytes. This finding also indicates that astrocyte clustering
310 requires multiple mitochondrial fission-deficient astrocytes to be adjacent to occur, as single
311 shDrp1 astrocytes with decreased Cx43 expression did not cluster with the neighboring wild-type
312 astrocytes. These data reveal that Drp1 knockdown results in a profound reduction of Cx43 protein
313 expression in astrocytes. Importantly, this effect of shDrp1 is Cx43 specific as we did not observe
314 a change in the levels of Cx30, another gap junction protein which is also expressed by astrocytes
315 (Sup. Fig. 3F). These results also suggest that Drp1-mediated Cx43 expression and/or localization
316 could be linked to the observed clustering phenotype of Drp1 knockdown astrocytes.

317

318 **Astrocyte-specific Drp1 knock out induces astrocyte reactivity**

319 To understand the impact of Drp1 loss in all astrocytes during cortical development, we utilized a
320 conditional (floxed) allele of mouse Drp1 (Wakabayashi et al., 2009a) which we crossed with the
321 tamoxifen-inducible astrocytic Cre-driver mouse Aldh1l1-CreERT2 (Srinivasan et al., 2016). A
322 tdTomato-floxed reporter (Ai14) was also used to identify cells expressing Cre (Fig. 6A). To delete
323 Drp1 from developing astrocytes, tamoxifen was injected into the milk spot of pups at P1, P2, and
324 P3 and mice were collected for analyses at P21 (Fig. 6A). This approach resulted in a significant
325 reduction of Drp1 protein in Drp1 conditional knock-out (cKO) astrocytes compared to wild-type
326 control (cWT) by immunoblotting of isolated cortical astrocytes (Fig. 6B-C). Further, we found
327 Drp1 protein reduced within Cre-positive (tdTomato^{+}) astrocytes across all cortical layers by
328 immunohistochemistry, with an overall significant decrease in V1 cortex in Drp1 cKO astrocytes
329 compared to control (Sup. Fig. 4A-C). To assess the recombination efficiency in this model, we
330 stained for astrocyte-specific nuclear marker Sox9 and quantified the number of tdTomato^{+}/Sox9^{+}
331 double positive cells in proportion to the total number of Sox9+ cells in Drp1 cKO and cWT mice
332 (Sup. Fig. 4E). We found that Cre recombination was not significantly different between Drp1
333 cWT and cKO conditions, both were ~80% efficient in recombining cells (Sup. Fig. 4F). These

results show that Aldh1L1-CreERT2 with daily tamoxifen injections between P1-P3 can be used to significantly reduce astrocytic Drp1 expression in mice *in vivo*.

Because we found that shDrp1 decreased astrocyte distal process formation and caused astrocyte clustering in our sparse PALE manipulation model, we wondered how global loss of Drp1 in astrocytes via conditional deletion would affect astrocyte development and cortical homeostasis. We found an overall decrease in astrocyte density in the cortex by tdTomato^{+} soma count that was primarily driven by decreases in L1 and L6 astrocytes in Drp1 cKO mice compared to control (Fig. 6D-E). Whole cortical quantification of astrocyte-specific nuclear marker Sox9 also confirmed a slight but significant decrease in overall astrocyte density (Sup. Fig. 4E, G). The decrease in astrocyte density did not impact overall cortical thickness (Sup. Fig. 4D). Next, we quantified tdTomato^{+} signal by immunohistochemistry as a proxy for astrocyte coverage and found that loss of Drp1 in cKO astrocytes significantly decreased their process coverage across the cortex compared to cWT, with the greatest coverage loss found in L5 and L6 astrocytes (Fig. 6F). Given that our astrocyte coverage analysis was normalized by astrocyte density, these data suggest this significant reduction in cortical astrocyte coverage is driven by the loss of astrocyte processes formation in Drp1 cKO.

Astrocytes modify their morphology and coverage of the cortex under disease and injury conditions (Fiebig et al., 2019; Oberheim et al., 2008). Further, mature cortical astrocytes express low GFAP protein under homeostatic conditions but increase their GFAP expression upon entering a reactive state (Middeldorp and Hol, 2011). Importantly, astrocyte reactivity is accompanied by shifts in both metabolic state and mitochondrial dynamics (Cassina et al., 2025; Rahman and Suk, 2020). Because we found morphology and coverage abnormalities in astrocyte-specific Drp1 cKO mice, we next tested whether the astrocytes in these brains became reactive. To do so, we performed immunohistochemistry for GFAP in Drp1 cKO and cWT cortices, and quantified changes in their GFAP density and coverage (Fig. 6D). We found that Drp1 cKO mice had significantly increased cortical GFAP expression predominantly in the mid layers (L2/3, L4, and L5) compared to control (Fig. 6G-H). Next, we measured mRNA levels of six markers of astrocyte reactivity in isolated astrocytes from Drp1 cKO and cWT mice. We found a significant upregulation of four out of six markers- GFAP, vimentin, LCN2, and Cxcl10 (Fig. 6I-L), a trending increase of Serpina3n, and no significant difference in Cp mRNA levels (Sup. 4H-I). These findings indicate that mitochondrial fission maintains astrocyte homeostasis during development

365 and suggest that developmental conditional deletion of Drp1 in astrocytes induces cortical
366 astrocyte reactivity *in vivo*.

367

368 **Astrocytic Drp1 loss disrupts astrocyte organization and dysregulates PAP protein**
369 **expression *in vivo***

370 To determine if conditional deletion of Drp1 in cortical astrocytes disrupted astrocyte organization
371 as we previously observed in our sparse PALE knockdown model (Fig. 5), we quantified both
372 nearest neighbor and multiple neighbor distances between tdTomato$^+$ somas in the cortices of cKO
373 and cWT mice (Fig. 7A). We found that in Drp1 cKO mice, astrocytes displayed significant
374 decreases in nearest neighbor distance (Fig. 7B), similar to the astrocyte clustering observed in our
375 sparse Drp1 KD model. Further, quantification of distances between multiple astrocyte neighbors
376 revealed that Drp1 cKO astrocytes have a greater variability in distances to their neighbors
377 compared to cWT astrocytes (Fig. 7C), indicating Drp1 cKO astrocytes have an unevenly
378 dispersed distribution of astrocyte somas compared to cWT. These data identify a disorganization
379 in cortical astrocytes in the absence of Drp1. Taken together, these results are in line with our
380 findings using shRNA constructs and PALE (Fig. 5) and show that loss of Drp1 in developing
381 astrocytes disrupts cortical astrocyte organization *in vivo*.

382 Given the robust disruption to astrocyte organization in Drp1 cKO mice, we next tested how Cx43
383 expression was impacted in Drp1 cKO astrocytes compared to cWT. To do so, we stained for Cx43
384 in the cortex and found that Drp1 cKO astrocytes displayed a heterogeneous and uneven
385 expression of Cx43, with some astrocytes apparently expressing almost no Cx43 while others
386 expressed wild-type or higher levels of the protein compared to the more even distribution of Cx43
387 in cWT cortices (Fig. 7D). Indeed, quantification of Cx43 signal showed that while there was no
388 change in average Cx43 expression between genotypes (Fig. 7E), there was significant increase in
389 the variance of Cx43 expression in Drp1 cKO astrocytes compared to cWT (Fig. 7F). We
390 quantified this heterogeneity by comparing the histogram of Cx43 expression per astrocyte and
391 found that Drp1 cKO astrocytes had a significantly altered distribution of Cx43 expression (Fig.
392 7G). This heterogeneous expression of cortical Cx43 protein *in situ* led us to investigate how Cx43
393 mRNA and protein expression may be disrupted in Drp1 cKO astrocytes. To do so, we
394 immunopurified astrocytes from the cortex and measured mRNA and protein levels of Cx43. Cx43

395 mRNA levels were unchanged in Drp1 cKO isolated astrocytes compared to cWT (Fig. 7H).
396 Interestingly, immunoblotting for Cx43 in isolated astrocytes demonstrated a robust decrease of
397 Cx43 full-length (FL) protein as well as its internally translated smaller isoforms in Drp1 cKO
398 astrocytes compared to cWT (Fig. 7I). Importantly, the trafficking of Cx43-FL to the cell
399 membrane to carry out its gap junction and cell-adhesion functions is regulated by its C-terminal
400 isoform, Cx43-20k (Smyth and Shaw, 2013). Both Cx43-FL and Cx43-20k protein levels were
401 significantly decreased in Drp1 cKO astrocytes compared to cWT (Fig. 7J-K). These findings
402 indicate that loss of Drp1 dysregulates Cx43 protein, but not mRNA, expression in astrocytes *in*
403 *vivo*.

404 Lastly, we tested how Drp1 loss impacts the abundance of other astrocyte membrane proteins
405 known to be localized to perisynaptic astrocyte processes (PAPs). To do so, we immunopurified
406 astrocytes from the cortices of cWT and cKO mice and measured protein levels of glutamate-
407 aspartate transporter (GLAST), glutamate transporter-1 (Glut1), and the inwardly rectifying
408 potassium channel Kir4.1 (Pajarillo et al., 2019; Takumi et al., 1995) by immunoblotting (Fig. 7L,
409 N, P). Intriguingly, all three PAP proteins were significantly decreased in isolated Drp1 cKO
410 astrocytes compared to control (Fig. 7M, O, Q), potentially due to the loss of distal astrocyte
411 processes that house these PAP proteins (Fig. 4C, Fig. 6F). These data indicate that mitochondrial
412 fission regulates PAP protein expression, including but not limited to Cx43, in developing
413 astrocytes. However, Drp1 cKO astrocytes lose Cx43 protein levels to a much greater degree
414 (reduced to <10% of cWT) than other PAP proteins (~70-50% of cWT), suggesting Cx43
415 homeostasis is more vulnerable to aberrant mitochondrial fission in astrocytes. Taken together,
416 these data suggest that Drp1-induced mitochondrial fission is required for proper PAP formation,
417 PAP protein expression, and the establishment of astrocyte organization in the cortex.

418

DISCUSSION

Astrocytes require a highly complex morphology to perform essential roles in brain development. They ramify into hundreds of thousands of fine processes enabling their functional interaction with synapses, neighboring astrocytes, and other brain cells. Distal mitochondria locally interact with the cytoskeleton to regulate branch morphology in compartmentalized cells such as neurons (Courchet et al., 2013; Smith and Gallo, 2018), but the roles of mitochondria in fine astrocyte processes are largely unknown. Mature astrocytes were historically believed to be predominantly glycolytic (Pellerin and Magistretti, 1994), not depending on mitochondrial respiration for their own survival (Supplie et al., 2017), and instead using their mitochondria to provide metabolic support for neurons (Pellerin et al., 1998). Indeed, astrocyte mitochondria have recently emerged as gatekeepers of several biological processes that maintain brain homeostasis including regulation of blood-brain barrier remodeling, neuroinflammation, and neurodegeneration (Göbel et al., 2019; Ignatenko et al., 2018; Motori et al., 2013; Popov et al., 2023). While these studies introduce astrocytic mitochondria as key regulators of brain function, the cell-intrinsic roles of mitochondria in astrocyte and brain development are not well understood.

Our findings elucidate a previously unknown role for mitochondrial fission in regulating distal astrocyte process morphogenesis and astrocyte organization in the developing mouse cortex. We show that astrocytes undergo robust mitochondrial division to predominantly occupy distal astrocyte processes during postnatal cortical development. Inhibiting mitochondrial fission by silencing Drp1, reduces mitochondrial occupancy of distal astrocyte processes and diminishes peripheral astrocyte branch formation specifically, without affecting overall astrocyte territory size or growth. Functionally, Drp1-induced mitochondrial fission is essential for the establishment of an organized astrocyte network and proper expression of PAP proteins including Cx43. Finally, global Drp1 loss in developing astrocytes induces cortical astrocyte reactivity, indicating that mitochondrial fission, distal mitochondrial localization, and astrocyte fine process formation are required for proper astrocyte development.

Several recent studies have elucidated astrocyte-neuron and astrocyte-astrocyte cell adhesion-based mechanisms that instruct astrocyte morphogenesis (Baldwin et al., 2021; Stogsdill et al., 2017; Takano et al., 2020; Tan et al., 2023; Zipursky et al., 2024). Curiously, loss of these cell-adhesions often concurrently disrupts both astrocyte territory formation and complexity of distal

449 astrocyte processes. Here we identify an organelle-driven mechanism that regulates peripheral
450 astrocyte process morphogenesis independently from the development of higher order astrocyte
451 processes and overall astrocyte size. The specificity of mitochondrial fission in regulating distal
452 astrocyte process development could be attributed to their actin-rich cytoskeletal make-up which
453 is distinct from larger processes. Primary astrocyte processes, which determine territory size,
454 contain mainly intermediate filaments and microtubules (Haseleu et al., 2013). In other cell types,
455 local mitochondrial ATP has been shown to fuel actin polymerization (Cunniff et al., 2016). Thus,
456 it is possible that mitochondrial fission facilitates the recruitment of mitochondria into actin-rich
457 distal astrocyte processes to supply local ATP required for actin polymerization during
458 morphogenesis. In the absence of mitochondrial fission, the mislocalization of mitochondria away
459 from peripheral, fine astrocyte branchlets could impair actin-cytoskeleton dynamics during
460 morphogenesis. Because these peripheral astrocyte processes are critical components of the
461 tripartite synapse, future work is needed to elucidate the role of astrocyte mitochondrial fission in
462 proper synapse formation and function.

463 Our study establishes the role of Drp1 and mitochondrial fission in astrocyte organization in the
464 cortex, and this disruption is likely accompanied by tiling defects. While the molecular
465 mechanisms that drive astrocyte domain formation and tiling remain largely unknown, we know
466 that proper organization of astrocyte networks is functionally necessary for brain development and
467 health. A recent study identified an astrocyte-astrocyte cell-adhesion molecule, HepaCAM, that
468 controls the establishment of non-overlapping astrocyte domains through cis interactions with
469 neighboring astrocytes and regulation of Cx43 localization (Baldwin et al., 2021). In our study,
470 both sparse knockdown and conditional deletion of Drp1 in astrocytes led to dysregulation of Cx43
471 protein expression and concurrent disruption of astrocyte organization in the cortex. These results
472 support previous findings that both Cx43 abundance and stability are critical for the proper
473 migration of astrocytes and even dispersion of the astrocyte network (Lagos-Cabré et al., 2019;
474 Wiencken-Barger et al., 2007), and reveal this process is regulated at least in part by astrocyte
475 mitochondrial fission during cortical development. Additionally, mitochondrial fission itself has
476 been shown regulate cell migration in immune cells, cancer cells, and neural progenitor cells (da
477 Silva et al., 2014; Kim et al., 2015; Paupe and Prudent, 2018). Thus, it is possible that Drp1 loss
478 could directly, or synergistically with Cx43 reduction, disrupt astrocyte migration and organization
479 in our model. Future work will need to investigate whether the relationship between Drp1, Cx43,

480 and astrocyte organization is direct or indirect, particularly because we found other PAP proteins
481 were also reduced in Drp1 cKO astrocytes. Lastly, while our study establishes mitochondrial
482 fission is necessary for proper Cx43 protein expression in astrocytes, functional gap junction
483 coupling studies will reveal whether Drp1 regulates astrocyte-network communication via gap
484 junctions.

485 How could Drp1-induced mitochondrial fission modulate Cx43 protein levels in astrocytes?
486 Previous studies in cardiac cells found that the C-terminus of Connexin 43 is internally translated
487 to generate a small 20kDa Cx43 isoform (Cx43-20kDa), which is required for the trafficking of
488 full-length Cx43 (Cx43-FL) to the cell membrane (Smyth and Shaw, 2013). Loss of Cx43-20kDa
489 leads to degradation of mistrafficked Cx-43-FL (Xiao et al., 2020). Importantly, Cx43-20kDa can
490 abandon its canonical Cx43-FL trafficking roles and instead employ a Drp1-independent, actin-
491 based mechanism to induce mitochondrial fission in conditions of oxidative stress and
492 mitochondrial elongation (Shimura et al., 2021). Therefore, it is plausible that Drp1 loss in
493 astrocytes redirects Cx43-20kDa away from its Cx43-FL trafficking role in an attempt to rescue
494 dysfunctional mitochondrial fission, resulting in the degradation of mistrafficked Cx43-FL.
495 Furthermore, Cx43-20kDa has been previously detected in astrocytes and overexpression of
496 astrocytic Cx43-20kDa promotes neuronal survival and recovery in a rat model of traumatic brain
497 injury (Ren et al., 2020). These studies, coupled with our findings, suggest the Cx43/Drp1 axis
498 may be critical for brain development, brain disease, and neurotherapeutics.

499 One of the existing dogmas of astrocyte biology is that astrocyte reactivity is often accompanied
500 by increased mitochondrial fragmentation and decreased oxidative phosphorylation (Cassina et al.,
501 2025; Motori et al., 2013; Rahman and Suk, 2020). In fact, inhibition of mitochondrial fission has
502 been studied as a therapeutic target for reducing astrocyte reactivity and neurotoxicity in models
503 of neurodegenerative disorders such as ALS and Huntington's disease (Gollihue and Norris, 2020;
504 Gu et al., 2025; Reddy, 2014). Intriguingly, our study demonstrates an opposite relationship
505 between mitochondrial fission and astrocyte reactivity during postnatal cortical development-
506 inhibition of mitochondrial fission in astrocytes upregulates multiple markers of astrocyte
507 reactivity. This finding indicates active mitochondrial fission is temporally necessary for
508 maintaining astrocyte homeostasis, specifically during brain development. Indeed, developing and
509 mature astrocytes have distinct metabolic profiles (Zehnder et al., 2021), thus it is plausible that
510 mitochondrial fission may have differential effects on astrocyte metabolism, mitochondrial

511 function, and astrocyte reactivity during astrocyte development, maturation, or aging. Lastly, while
512 Drp1-null or neuron-specific conditional deletion of Drp1 during development is embryonically
513 or neonatally lethal in mice (Ishihara et al., 2009; Wakabayashi et al., 2009b), our astrocyte-
514 specific model of Drp1 loss did not affect mouse viability during the developmental timeframe of
515 this study. Future investigations extending beyond the postnatal developmental window will reveal
516 how astrocyte-specific Drp1 loss and astrocyte reactivity affect mouse behavior or physiology
517 long-term.

518 Finally, this study has important implications for understanding the pathology of neurological
519 diseases, particularly neurodevelopmental diseases with Drp1 dysfunction. Indeed, point
520 mutations in human Drp1 cause encephalopathy due to defective mitochondrial and peroxisomal
521 fission-1 (EMPF1), a devastating disorder that presents with microcephaly, developmental delay,
522 refractory epilepsy, or lethal infantile encephalopathy (Fahrner et al., 2016; Lhuissier et al., 2022;
523 Liu et al., 2021; Vanstone et al., 2016). While much research has focused on the disruption of
524 excitation/inhibition (E/I) balance and neuronal pathogenesis of EMPF1 (Casillas-Espinosa et al.,
525 2012; Ke et al., 2023), our results reveal how Drp1 dysfunction in astrocytes alone can
526 fundamentally disrupt cortical development through astrocyte morphogenesis and organization
527 deficits. Decreased distal astrocyte process development could contribute to diminished tripartite
528 synapse formation (Stogsdill et al., 2017), subsequently disrupting the E/I balance. Furthermore,
529 while loss of astrocyte tiling has been reported in models of epilepsy (Oberheim et al., 2008), it
530 has been unclear whether the phenotype is causative or a consequence of disease. Our findings
531 suggest endogenous loss of astrocytic Drp1 is sufficient to cause astrocyte reactivity, which is a
532 hallmark of many neurological disorders, underscoring the translational importance of astrocyte
533 mitochondrial fission in neuropathology. In future studies, it will be interesting to investigate
534 whether astrocyte-specific Drp1 loss causes synaptic E/I imbalance deficits associated with human
535 *DNM1L* mutations. In conclusion, we show a novel role of Drp1-induced mitochondrial fission in
536 astrocyte peripheral process morphogenesis and in regulating the establishment of an organized
537 astrocyte network, demonstrating astrocyte mitochondria are essential instructors of proper brain
538 development.

539 **FIGURE LEGENDS**

540 **Fig.1: Mitochondria increase in number and decrease in size during cortical astrocyte**
541 **morphogenesis *in vivo*.** (A) Schematic of Postnatal Astrocyte Labeling by Electroporation
542 (PALE). (B) Representative images of V1 astrocytes expressing mCherry-CAAX (magenta, top
543 panels) and their EGFP mitochondria (green, bottom panels) at P4, P7, P14, and P21. Scale bar:
544 10 µm. Super-plots for the quantification of (C) astrocyte cell volume, (D) total mitochondrial
545 volume per cell, (E) mitochondrial volume normalized to cell volume, (F) average mitochondrial
546 number per cell, and (G) average mitochondrial size per cell from P4-P21. N=3-4 male and female
547 mice/timepoint (large circled data points), n= 2-6 cells/mouse, 10-13 cells total/timepoint (small
548 gray data points). Data are presented as mean ± SEM. Nested one-way ANOVA with Tukey post-
549 hoc test.

550 **Fig. 2: Mitochondria occupy fine astrocyte processes concurrently with astrocyte**
551 **morphological arborization *in vitro*.** (A) Schematic of astrocyte-neuron co-culture assay. (B)
552 Representative images of rat astrocytes transfected with EGFP (green, top panels) and MitoDsRed
553 (magenta, middle panels) from 4 to 48 hours in co-culture with cortical neurons. Inset (bottom
554 panels) of distal astrocyte processes (green) housing mitochondria (magenta) at the leading edge
555 of growing processes (white arrowheads) from 4 to 48 hours in culture. Scale bars: 20 µm. (C)
556 Overview of Seg_Astro image analysis pipeline. (D) Astrocyte secondary, fine/distal, and terminal
557 branch number at 4 vs. 48 hours in culture. n = 10-12 cells per timepoint from one experiment.
558 Unpaired two-tailed t-test. (E) Total astrocyte mitochondria number, and (F) average mitochondrial
559 size in secondary, fine/distal, and terminal astrocyte branches from 4 to 48 hours in culture. n =
560 10-12 cells per timepoint from one experiment. Data are presented as mean ± SEM. One-way
561 ANOVA with Tukey post-hoc test.

562 **Fig 3: Drp1-induced mitochondrial fission is required for fine astrocyte process formation**
563 **and mitochondrial localization *in vitro*.** (A) Schematic of Drp1 in mitochondrial fission. (B)
564 Drp1 domain structure noting K38E mutation in the GTPase domain. (C) Representative images
565 of rat astrocytes transfected with shControl or shDrp1 (green) and MitoDsRed (magenta) (top
566 panels) co-cultured on neurons (unlabeled), with a MitoDsRed mask (lower panels) noting
567 hyperfused/elongated mitochondria in shDrp1 astrocytes (red arrowheads). Scale bars: 40 µm. (D)
568 Representative images of rat astrocytes transfected with shRNA targeting Drp1 (shDrp1) or a

569 scrambled control (shControl) (first column) co-cultured on neurons (unlabeled), and their
570 mitochondria (second column) across primary, secondary, fine, and terminal astrocyte process
571 types. Scale bar: 20µm. (E) Super-plotted quantification of average mitochondrial number in
572 secondary, fine, and terminal branches from shControl vs. shDrp1 astrocytes. (F) Quantification
573 of primary, secondary, fine, and terminal branch numbers from shControl and shDrp1 astrocytes.
574 Data are mean ± S.E.M. n = 4 independent experiments (large circles), 10
575 cells/condition/experiment (small gray dots). Nested t-test. (G) Representative images of rat
576 astrocytes transfected with shControl (green), shDrp1 (green), shDrp1 (green)+ hDrp1-YFP
577 (magenta), or shDrp1 (green)+ hDrp1-K38E-CFP (magenta). Scale bar: 40µm. (H) Quantification
578 of total primary, (I) secondary, (J) fine, and (K) terminal branch number in astrocytes across the 4
579 conditions from (G). Data are mean ± S.E.M. n = 3 independent experiments (large circles), 10
580 cells/condition/experiment (small gray dots). Nested One-way ANOVA with Tukey post-hoc test.

581 **Fig 4: Mitochondrial fission, not fusion nor transport, is required for distal astrocyte process**
582 **morphogenesis *in vivo*.** (A, E, I) Schematic of mitochondrial fission, fusion, and transport
583 mediated by Drp1, Mfn1, and Miro1, respectively. (B-D, F-H, J-L) Representative images of V1
584 P21 astrocytes expressing mCherry-CAAX-tagged shRNA (magenta) against Drp1 (shDrp1),
585 Mfn1 (shMfn1), Miro1 (shMiro1), or scrambled control (shControl) and their EGFP mitochondria
586 (green). Scale bar, 10µm. (B, F, J) Astrocyte territory (cyan) and quantification, (D, G, K) NIV
587 reconstructions (cyan) and quantification, and (D, H, L) distal mitochondrial volume (green within
588 cyan ROI) and quantification in shControl, shDrp1, shMfn1, and shMiro1 conditions, respectively.
589 N= 4-5 male and female mice/condition (large circles), n=2-4 cells/mouse, 10-15 cells
590 total/condition (small gray dots). Data are mean ± S.E.M. Nested t-test.

591 **Fig 5: Drp1 controls cortical astrocyte organization during postnatal development.** (A)
592 Representative images of V1 mouse cortices with astrocytes expressing mCherry-CAAX-tagged
593 shRNA (magenta) against Drp1 (shDrp1) or scrambled control (shControl) and their EGFP
594 mitochondria (green) at P7, P14, and P21. Scale bar, 200µm. (B) Quantification of astrocyte
595 individual or cluster area per field of view at P7, P14, P21. N=3-4 male and female mice/condition
596 (big circles), 3 cortical sections/mouse (small gray dots). Data points are mean ± S.E.M. Nested t-
597 test. (C) Representative images of shControl (top) and shDrp1 (bottom) P21 astrocytes expressing
598 mCherry-CAAX shRNAs (magenta) and stained with Sox9 (green). Yellow arrows note Sox9+
599 astrocytic nuclei within mCherry+ astrocytes. Scale bar, 40µm. (D) Quantification of number of

600 Sox9+ astrocyte nuclei and (E) nearest neighbor distance between astrocytes per astrocyte cluster
601 in P21 shControl and shDrp1 astrocytes. N=4-5 male and female mice/condition (large circles),
602 n=2-6 cells or clusters/condition, 20 cells or clusters total/condition (small gray dots). Data are
603 mean ± S.E.M. Nested t-test. (F) Representative images of V1 astrocytes expressing mCherry-
604 CAAX (magenta) and shControl (top row) or shDrp1 (bottom two rows, shDrp1 clusters or single
605 astrocytes) stained with Cx43 (cyan) at P21. Scale bars, 20µm. (G) Quantification of Connexin43
606 expression within mCherry-CAAX astrocytes. N=6 male and female animals/condition (large
607 circles), n=1-8 cells or clusters/animal, 10-25 cells total/condition (small gray dots). Data are mean
608 ± S.E.M. Nested one-way ANOVA.

609 **Fig 6: Astrocyte-specific Drp1 cKO induces cortical astrocyte reactivity.**

610 (A) Overview of astrocyte-specific conditional Drp1 knockout mouse breeding strategy and
611 timeline of tamoxifen administration. (B) Representative immunoblot for Drp1 from immuno-
612 purified astrocytes. COX4, a mitochondrial protein, serves as a loading control. (C) Quantification
613 of Drp1 protein in isolated cKO and cWT astrocytes. N=3 mice/condition. Data are mean ± S.E.M.
614 Unpaired, two-tailed t-test. (D) Representative images of Drp1 cWT and cKO V1 cortices at P21
615 with tdTomato$^+$ astrocytes (magenta, first column), stained for GFAP (green, second column), and
616 merge (third column). Scale bar, 100µm. Zoom merge (last column). Scale bar, 20µm. (E)
617 Quantification of cortical tdTomato$^+$ soma count of astrocyte density, (F) tdTomato$^+$ astrocyte
618 coverage normalized to astrocyte density, (G) GFAP soma count, and (H) GFAP coverage
619 normalized to astrocyte density per layer in Drp1 cKO compared to cWT. N=4 male and female
620 mice/condition, 2-3 cortical images/mouse. Data are mean ± S.E.M. Two-way ANOVA with
621 Sidak's multiple comparisons test. Quantification of (I) GFAP, (J) Vimentin, (K) LCN2, and (L)
622 Cxcl10 mRNA from isolated Drp1 cKO and cWT astrocytes. N=2-6 male and female
623 mice/condition. Data are mean ± S.E.M. Unpaired two-tailed t-test.

624 **Fig 7: Astrocytic Drp1 loss dysregulates astrocyte organization and PAP protein expression**
625 **in the mouse cortex.** (A) Diagram of astrocyte organization analysis by nearest and multiple
626 neighbor distance quantification. (B) Violin plot of nearest neighbor average distance between
627 tdTomato$^+$ somas across V1 cortex of Drp1 cWT and cKO mice. N=4 male and female
628 mice/condition (large circles), ~200 distances per image, 2-3 cortical images/mouse. Data are
629 mean ± S.E.M. Nested t-test. (C) Distribution of average distances to multiple (9) neighbors. N=4

630 male and female mice/condition, ~200 distances per image, 2-3 images/mouse. Kolmogorov-
631 Smirnov test. (D) Representative images of Drp1 cWT and cKO V1 cortices with tdTomato^{+}
632 astrocytes (magenta) stained with Cx43 (cyan) at P21. Scale bar, 100µm. Zoom merge (last
633 column). Scale bar, 20µm. Quantification of (E) individual (F) variance, and (G) distribution of
634 Cx43 mean gray value per astrocyte in Drp1 cKO and cWT mice. N=4 male and female
635 mice/condition, n= 15-30 mid-layer astrocytes (L2/3, L4, L5) per animal from 2-3 section
636 images/animal. Nested t-test for (E), Unpaired, two-tailed t-test for (F), and Kolmogorov-Smirnov
637 test for (G). (H) Quantification of Cx43 mRNA from isolated cKO and cWT astrocytes. N=4-6
638 mice/condition. Data are mean ± S.E.M. Unpaired two-tailed t-test. (I) Representative immunoblot
639 of isolated astrocytes for Cx43 showing its full-length form at 40kDa and its 20kDa isoform using
640 COX4 as loading control. (J) Quantification of full-length Cx43 protein, (K) Cx43-20kDa isoform
641 protein in isolated cKO and cWT astrocytes. N=3 mice/condition. Data are mean ± S.E.M.
642 Unpaired, two-tailed t-test. Representative immunoblots for (L) GLAST, (N) Glut1, and (P) Kir4.1
643 from immuno-purified astrocytes from Drp1 cWT and cKO mice. COX4, a mitochondrial protein,
644 serves as a loading control. Quantification of (M) GLAST, (O) Glut1, and (Q) Kir4.1 protein in
645 isolated cKO and cWT astrocytes. N=3-4 mice/condition. Data are mean ± S.E.M. Unpaired, two-
646 tailed t-test.

647 **Supplemental Figure 1: Validation of shRNA tools**

648 (A) Schematic of shDrp1 sequence aligned to the mouse, rat, and human genome. (B) Drp1 relative
649 mRNA expression in control and shDrp1 transfected mouse 3T3 cells. (C) Schematic of shMiro1
650 and shMfn1 sequences aligned to the mouse genome. (D) Miro1 and (E) Mfn1 relative mRNA
651 expression in control and shDrp1 transfected mouse 3T3 cells. Data are mean ±S.E.M. n = 3
652 independent experiments. Unpaired two-tailed t-test.

653 **Supplemental Figure 2: Genetic manipulation of mitochondrial dynamics in vivo alters**
654 **mitochondria number and size**

655 (A) Representative images (left column) and Imaris reconstructions (right column) of V1 P21
656 astrocyte mitochondria expressing EGFP (green) and shRNA against Drp1 (shDrp1), Mfn1
657 (shMfn1), Miro1, (shMiro1) or scrambled control (shControl). Scale bar, 10µm. **(B-D)**
658 Quantification of astrocyte average mitochondrial number (left graphs) and average mitochondrial
659 size (right graphs) in shDrp1, shMfn1, and shMiro1 conditions, respectively. N=4-5 male and

660 female mice/condition (large circles), n=2-4 cells/mouse, 10-15 cells total/condition (small gray
661 dots). Data are mean ± S.E.M. Nested t-test. (E) Representative images of Imaris reconstructed V1
662 P21 astrocytes expressing mCherry-CAAX-tagged shRNA (magenta) against Drp1 (shDrp1),
663 Mfn1 (shMfn1), Miro1, (shMiro1) or scrambled control (shControl) and their EGFP mitochondria
664 (green). Scale bar, 10µm. Quantification of total mitochondrial volume normalized to cell volume
665 in (F) shDrp1, (G) shMfn1, and (H) shMiro1 conditions, respectively. N=4-5 male and female
666 mice/condition (large circles), n=2-4 cells/mouse, 10-15 cells total/condition (small gray dots).
667 Data are mean ± S.E.M. Nested t-test.

668

669 **Supplemental Figure 3: Characterization of shDrp1-induced astrocyte clustering**

670 (A) Overview of PALE combined with EdU labeling. (B) Representative images of V1 cortices
671 with astrocytes expressing mCherry-CAAX shRNA (red) against Drp1 (shDrp1) or scrambled
672 control (shControl) and EdU labeling (magenta) at P4 and P14. Scale bar, 200µm. (C)
673 Quantification of Edu+ cells in shControl or shDrp1 cortices at P4, P8, P10, P12, and P14. N=3-4
674 male and female mice/condition, 3 cortical section images/mouse. Data points are timepoint
675 averages ± S.E.M. Two-way ANOVA with Sidak's multiple comparisons test. (D) Representative
676 images of V1 cortices with astrocytes expressing mCherry-CAAX shRNA (magenta) against Drp1
677 (shDrp1) or scrambled control (shControl) at 2 months and 6 months. Scale bar, 200µm. (E)
678 Quantification of astrocyte cell or cluster area per field of view at 2 and 6 months. N=3 male and
679 female mice/condition (large circles), 3 cortical section images/mouse (small gray dots). Data
680 points are mean ± S.E.M. Nested t-test. (F) Representative images of V1 astrocytes from 3 mice
681 per condition expressing mCherry-CAAX and shControl (top two rows) and shDrp1 (bottom two
682 rows) stained with an antibody against Cx30 (cyan) at P21. Scale bars, 20µm.

683 **Supplemental Figure 4: Astrocyte-specific Drp1 cKO mouse characterization**

684 (A) Representative images of Drp1 cWT and cKO V1 cortices with tdTomato^{+} astrocytes
685 (magenta) stained with Drp1 (yellow) and showing Drp1 masked by tdTomato (last column) at
686 P21. Scale Bar, 40µm. (B-C) Quantification of Drp1 mean gray value within tdTomato area
687 normalized to astrocyte density per cortical layer (B) and across the whole cortex (C). N=3-4 male
688 and female mice/condition, 2-3 cortical images/mouse. Data points are mean ± S.E.M. Two-way
689 ANOVA with Sidak's multiple comparisons test for B, and Unpaired, two-tailed t-test for C. (D)

690 Quantification of cortical thickness in Drp1 cKO compared to cWT mice. N=4 male and female
691 mice/condition (large circles), n=2-3 cortical images/mouse (small gray dots). Data are mean ±
692 S.E.M. Unpaired, two-tailed t-test. (E) Representative images of Drp1 cWT and cKO V1 cortices
693 with tdTomato^{+} astrocytes (magenta) stained with Sox9 (green) at P21. Scale Bar, 100µm.
694 Quantification of (F) percent Sox9 and tdTomato double positive astrocytes out of total Sox 9
695 positive nuclei, and (G) total Sox 9 positive nuclei per cortical field of view in Drp1 cWT and cKO
696 mice. N= 3 male and female mice/condition (large circles), n=3 cortical images/mouse (small gray
697 dots). Data points are mean ± S.E.M. Nested t-test. Quantification of (H) Serpina3n and (I) Cp
698 mRNA from immuno-purified astrocytes from Drp1 cWT and cKO mice. N=6 male and female
699 mice/condition. Data are mean ± S.E.M. Unpaired two-tailed t-test.

MATERIALS AND METHODS

Resource availability

Further information and requests for resources and reagents should be directed to and will be fulfilled by Cagla Eroglu (cagla.eroglu@duke.edu).

Materials availability

The reagents generated in this study are available without restriction.

Data and code availability

The raw data and analyses generated during this study can be accessed on Zenodo at DOI: 10.5281/zenodo.15328429. The Seg_Astro code can be found at https://zenodo.org/records/15311182. Any additional information can be requested from the lead contact.

Animal studies

All mice and rats were used in accordance with the Institutional Animal Care and Use Committee (IACUC) and with oversight by the Duke Division of Laboratory Animal Resources (IACUC Protocol Numbers A117-20-05 and A103-23-04). All animals were housed under typical 12-hour light/dark cycles. Aldh1l1-Cre/ERT2 BAC transgenic (RRID:IMSR_JAX:029655) and ROSA-td-Tomato Ai14 (RTM) (RRID:IMSR_JAX:007914) lines were obtained through Jackson Laboratory. Wild-type CD1 mice (RRID: IMSR_CRL:022) used for PALE and CD1 (Sprague-Dawley) IGS rats (RRID: IMSR_CRL:400) used for primary culture preps were purchased from Charles River Laboratories. Rosa26-lsl-mito-EGFP (RRID:IMSR_JAX:021429) were previously described (Agarwal et al., 2017). Drp1 conditional knockout mice were previously described and were a gift from the Sesaki Laboratory (Wakabayashi et al., 2009a). Mice and rats of both sexes were included in all experiments. Sex was not an influence on any of the experimental outcomes.

Primary Cultures

Cortical Neuron Isolation and Culture Purified (glia-free) rat cortical neurons were prepared as described previously (Stogsdill et al., 2017). In brief, cortices from P1 rat pups of both sexes

726 (Sprague Dawley, Charles River Laboratories, SD-001) were micro-dissected, digested in papain
727 (~7.5 units/mL) at 33°C for 45 minutes, triturated in low and high ovomucoid solutions,
728 resuspended in panning buffer (DPBS (Gibco 14287) supplemented with BSA and insulin) and
729 passed through a 20 µm mesh filter (Elko Filtering 03-20/14). Filtered cells were incubated on
730 negative panning dishes coated with Bandeiraea Simplicifolia Lectin 1 (x2), followed by goat anti-
731 mouse IgG+IgM (H+L) (RRID: AB_2338451), and goat anti-rat IgG+IgM (H+L)
732 (RRID:AB_2338094) antibodies, then incubated on positive panning dishes coated with mouse
733 anti-L1 (RRID:AB_528349) to bind cortical neurons. Adherent cells were collected by forceful
734 pipetting with a P1000 pipette. Isolated neurons were pelleted (11 min at 200 g) and resuspended
735 in serum-free neuron growth media (NGM; Neurobasal, B27 supplement, 2 mM L-Glutamine, 100
736 U/mL Pen/Strep, 1 mM sodium pyruvate, 4.2 µg/mL Forskolin, 50 ng/mL BDNF, and 10 ng/mL
737 CNTF). 100,000 neurons were plated onto 12 mm glass coverslips coated with 10 µg/mL poly-D-
738 lysine (PDL, Sigma P6407) and 2 µg/mL laminin and incubated at 37°C in 10% CO2. On day in-
739 vitro (DIV) 2, half of the media was replaced with NGM Plus (Neurobasal Plus, B27 Plus, 100
740 U/mL Pen/Strep, 1 mM sodium pyruvate, 4.2 µg/mL Forskolin, 50 ng/mL, BDNF, and 10 ng/mL
741 CNTF) and AraC (10 µM, Sigma, C1768) was added to stop the growth of proliferating
742 contaminating cells. On DIV 3, all of the media was replaced with NGM Plus. Neurons were fed
743 on DIV 6 and DIV 9 by replacing half of the media with NGM Plus. Detailed protocol can be
744 found at (https://www.protocols.io/view/glia-free-cortical-neuron-culture-36wgq3r35lk5/v1)

745 *Cortical Astrocyte Isolation and Culture* Rat cortical astrocytes were prepared as described
746 previously (Stogsdill et al., 2017). Briefly, P1 rat cortices from both sexes were micro-dissected,
747 papain digested, triturated in low and high ovomucoid solutions, and resuspended in astrocyte
748 growth media (AGM: DMEM (Gibco 11960), 10% FBS, 10 µM, hydrocortisone, 100 U/mL
749 Pen/Strep, 2 mM L-Glutamine, 5 µg/mL Insulin, 1 mM Na Pyruvate, 5 µg/mL N-Acetyl-L-
750 cysteine). Between 15-20 million cells were plated on 75 mm2 flasks (non-ventilated cap) coated
751 with poly-D-lysine and incubated at 37°C in 10% CO2. On DIV 3, removal of non-astrocyte cells
752 was performed by forcefully shaking closed flasks by hand for 10-15 seconds until only an
753 adherent monolayer of astrocytes remained. AraC was added to the media from DIV 5 to DIV 7 to
754 eliminate contaminating fibroblasts. On DIV 7, astrocytes were trypsinized (0.05% Trypsin-
755 EDTA) and plated into 12-well or 6-well dishes. On DIV 8, cultured rat astrocytes were transfected

with shRNA and/or expression plasmids using Lipofectamine LTX with Plus Reagent (Thermo Scientific, 15338100) per the manufacturer's protocol. Briefly, 1 µg (12-well) or 2 µg (6-well) total DNA was diluted in Opti-MEM containing Plus Reagent, mixed with Opti-MEM containing LTX (1:2 DNA to LTX) and incubated for 30 minutes. The transfection solution was added to astrocyte cultures and incubated at 37°C for 3 hours. On DIV 10, astrocytes were trypsinized, resuspended in NGM plus, plated (20,000 cells per well) onto DIV 10 neurons, and co-cultured for 48 hours. Detailed protocol can be found at (https://www.protocols.io/view/astrocyte-isolation-and-acm-production-261gedp57v47/v1).

Cell Lines

3T3 3T3 cells (RRID:CVCL_0594) used for shRNA validation experiments were cultured in DMEM supplemented with 10% fetal bovine serum, 100 U/mL Pen/Strep, 2 mM L-Glutamine, and 1 mM sodium pyruvate. Cells were incubated at 37°C in 5% CO2 and passaged every 2-3 days.

Plasmids

shRNA plasmids pLKO.1 puro plasmids containing shRNA against mouse/rat *Drp1* (TRCN0000321170; CTATAATGCATGCACTATTTA) was generated in this study. shRNA sequence was obtained from RNAi Consortium (TRC) via Dharmacon. A scrambled shRNA sequence was generated (GTTCTAAGTTCCGTGTTCAGG) and cloned into the pLKO.1 TRC cloning vector (Moffat et al., 2006) according to Addgene protocols (https://www.addgene.org/protocols/plko/). To generate pLKO.1 shRNA plasmids that express EGFP, CAG-EGFP was removed from pLenLox-shNL1-CAG-EGFP (Chih et al., 2006) and inserted between Kpn1 and Spel sites in pLKO.1 Puro, replacing the puromycin resistance gene in pLKO.1. Final constructs generated were pLKO.1-scrambled-GFP (RRID: Addgene_228736) and pLKO.1-shDrp1-GFP (RRID: Addgene_228737).

PiggyBac plasmids pGLAST-PBase was a gift from Dr. Joseph Loturco (Chen and LoTurco, 2012). shRNA sequences against mouse/rat *Miro1* (TRCN0000330651; TGGACTGTGCTTCGACGATTT), *Mfn1* (TRCN0000081400; GCAAGATTACAGGAGTTTCAA), and *Drp1* (see above *shRNA plasmids*) were obtained from

784 RNAi Consortium (TRC) via Dharmacon. A scrambled shRNA sequence was generated (see above
785 *shRNA plasmids*). To insert the hU6 promoter and shRNA in pPBCAG-mCherry-CAAX a DNA
786 fragment containing hU6 and shRNA was amplified from pLKO.1-shRNA using Phusion High-
787 Fidelity DNA Polymerase (NEB) with primers that introduced SpeI restriction sites (Forward
788 Primer: GGACTAGTCAGGCCCGAAGGAATAGAAG; Reverse Primer:
789 GGACTAGTGCCAAAGTGGATCTCTGCTG). PCR products were purified, digested with SpeI,
790 and ligated into pPBCAG-mCherry-CAAX at the SpeI restriction site. An analytical digest with
791 EcoRI followed by sequencing was used to confirm the orientation of the inserted DNA fragment.
792 Final plasmids generated were pPB-scrambled-mCherry-CAAX (RRID: Addgene_228738), pPB-
793 sDrp1-mCherry-CAAX (RRID: Addgene_228739), pPB-shMiro1-mCherry-CAAX (RRID:
794 Addgene_228741), and pPB-shMfn1-mCherry-CAAX (RRID: Addgene_228740).

795 *Other plasmids* hDrp1-YFP and hDrp1-K38E-CFP were gifts from Heidi McBride (König et al.,
796 2021) . Mito-DsRed was acquired from Addgene (RRID: Addgene_55838).

797 **Biochemical assays**

798 *mRNA extraction and cDNA preparation* Cells stored in TRIzol (#15596026; Invitrogen) were
799 brought to room temperature and resuspended in a final volume of 1 ml of TRIzol. 200 µl of
800 chloroform was added to each sample and mixed thoroughly. Samples were centrifuged at 12,000
801 g for 15 min at 4°C for phase separation and the clear aqueous phase was collected. 2 µl of
802 GlycoBlue Coprecipitant (15 mg/ml, #AM9515; Invitrogen) and 500 µl of isopropanol were added
803 to each sample, centrifuged at 12,000 g for 10 min at 4°C, precipitating RNA as a blue pellet. The
804 RNA pellet was rinsed in 75% ethanol, air-dried, and resuspended in 20 µl of nuclease-free water.
805 mRNA concentration in each sample was quantified via Qubit RNA HS Assay Kit (#Q32852;
806 Invitrogen). RNA samples were then diluted with nuclease-free water to match concentrations
807 across all samples. cDNA libraries were then generated by incubating the samples with qScript
808 cDNA SuperMix (#101414-102; VWR) and nuclease-free water for 5 min at 25°C, 30 min at 42°C,
809 and 5 min at 85°C. The resulting cDNA was then diluted appropriately with nuclease-free water
810 and stored at −80°C (https://www.protocols.io/view/mrna-extraction-and-cdna-preparation-
811 bp2l623n5gqe/v1) .

812 *Real-time qPCR* cDNA samples were plated in duplicate on a 96-well qPCR plate and incubated
813 with Fast SYBR Green Master Mix (#4385616; Applied Biosystems), nuclease-free water, and
814 the forward and reverse primers of interest at a ratio of 5 µl SYBR: 3 µl water: 0.5 µl forward
815 primer: 0.5 µl reverse primer: 1 µl sample. Each sample was plated twice to ensure technical
816 replicates. A no-cDNA sample (water with primers and Master Mix) served as a negative control.
817 Cycle threshold values were collected for each well and normalized to PPIA as a housekeeping
818 gene. (https://www.protocols.io/view/real-time-qpcr-j8nlk8mexl5r/v1). The sequences of forward
819 (F) and reverse (R) primers used (5′→ 3′) are:
820 Drp1: (F) TTACGGTTCCCTAAACTTCACG and (R) GTCACGGGCAACCTTTTACGA
821 Miro1: (F) TGGGCAGCACTGATAGAATAGA and (R) GCAAAGACCGTAGCACCAAAG
822 Mfn1: (F) CCTACTGCTCCTTCTAACCCA and (R) AGGGACGCCAATCCTGTGA
823 Cx43: (F) ACAGCGGTTGAGTCAGCTTG and (R) GAGAGATGGGGAAGGACTTGT
824 GFAP: (F) GGGGCAAAAGCACCAAAGAAG and (R) GGGACAACTTGTATTGTGAGCC
825 Vimentin: (F) CGTCCACACGCACCTACAG and (R) GGGGGATGAGGAATAGAGGCT
826 PPIA: (F) GAGCTGTTTGCAGACAAAGTTC and (R) CCCTGGCACATGAATCCTGG
827 LCN2: (F) TGGCCCTGAGTGTCATGTG and (R) CTCTTGTAGCTCATAGATGGTGC
828 Cxcl10: (F) CCAAGTGCTGCCGTCATTTTC and (R) GGCTCGCAGGGATGATTTCAA
829 Serpina3: (F) ATTTGTCCCAATGTCTGCGAA and (R) TGGCTATCTTGGCTATAAAGGGG
830 Cp: (F) CTTAGCCTTGGCAAGAGATAAGC and (R) GGCCTAAAAACCCTAGCCAGG

831 *Protein extraction and western blotting* Protein was extracted from cultured cells using RIPA lysis
832 buffer (ThermoFisher, 89900). Cells were washed twice with ice-cold DPBS and incubated on ice
833 in RIPA buffer for 5 minutes with occasional agitation. Cell lysates were collected, vortexed
834 briefly, and centrifuged at 4°C at high speed for 10 minutes to pellet non-solubilized material. The
835 supernatant was collected and stored at −80°C. To collect protein from astrocytes from Drp1 *cWT*
836 and *cKO* mice at P21, astrocytes were isolated following a modified version of the Magnetic
837 Activated Cell Sorting (MACS) protocol previously described (Holt et al., 2019). In brief, mice
838 were anesthetized with 200 mg/kg tribromoethanol (avertin) and perfused with TBS/Heparin,
839 cortices rapidly dissected, digested in papain (~7.5 units/mL) at 33°C for 45 minutes with pipette
840 trituration every 15 minutes. Then homogenates were resuspended in Magnetic Activated Cell
841 Sorting (MACS) buffer (0.002M EDTA, 0.2% milk peptone, 0.01M HEPES pH 7, 0.5% Glucose,

842 1X HBSS), and passed through a CellTrics 30 µm filter (Sysmex, 04-004-2326). Cortical cells
843 were then cleared from microglia by incubating with anti-CD11b human/mouse magnetic
844 microbeads (Miltenyi Biotec, 130-093-634) for 10 minutes at 4°C with rotation and passed through
845 an LS separation column (Miltenyi Biotec, 130-042-401) inserted into a Quadro MACS Multi
846 Stand magnetic stand (Miltenyi Biotec) followed by 3 washes with MACS buffer. Flowthrough
847 was then spun down and resuspended in MACS buffer and incubated with blocking buffer and
848 anti-ACSA2 mouse magnetic microbeads (Miltenyi Biotec, 130-097-678, RRID: AB_2894998)
849 for 30 minutes at 4°C with rotation to isolate astrocytes. Cell suspension was again passed through
850 a separation column inserted into a magnetic stand, rinsed 3 times with MACS buffer and column
851 retentate (ACSA2+ population, astrocytes) was pelleted. Supernatant was discarded and astrocyte
852 pellet was resuspended in RIPA buffer containing protease inhibitors (Roche, 4693132001) and
853 incubated with rotation at 4°C for 20 minutes. Lysate was centrifuged at max speed at 4°C for 10
854 minutes, supernatant collected and stored at −80°C.

855 Pierce Micro BCA Protein Assay Kit (Thermo Fisher, 23235) was used to determine protein
856 concentration, and lysates were subjected to western blot analysis and quantification using a
857 SimpleWestern Jess (ProteinSimple) automated immunoassay system with a 12-230kDa
858 Chemiluminescence Separation module (SM-W001) and associated manufacturer's protocol.
859 Primary antibodies used were: anti-Drp1 (Rabbit,1:10, RRID: AB_2895215), Connexin43 (Rabbit,
860 1:10, RRID:AB_2294590), COX4 (Rabbit, 1:10, RRID:AB_443304), GLAST (Rabbit, 1:150,
861 RRID:AB_2190597), GLUT1 (Rabbit, 1:30, RRID:AB_2809254), and Kir4.1 (Rabbit, 1:10,
862 RRID:AB_2040120).

863 **Immunocytochemistry**

864 Astrocyte-neuron co-cultures on glass coverslips were fixed on DIV 12 with warm 4% PFA for 7
865 minutes, washed 3 times with PBS, blocked in a blocking buffer containing 50% normal goat
866 serum (NGS) and 0.4% Triton-X 100 for 30 minutes, and washed in PBS. Samples were then
867 incubated overnight at 4°C in primary antibodies diluted in blocking buffer containing 10% NGS.
868 Primary antibodies used were: anti-GFP (Chicken, 1:1000, RRID:AB_10000240) and anti-RFP
869 (Rabbit, 1:1000, RRID:AB_2209751). Cells were then washed with PBS, incubated in Alexa-
870 Fluor conjugated secondary antibodies (Ck 594 RRID:AB_2534099; Rb 594, RRID:AB_2534079;

871 Ck 488 RRID:AB_2534096; Rb 488, RRID:AB_2925776; Rb 405, RRID:AB_2890548; Ms IgG1
872 647, RRID:AB_2535809) for 2 hours at room temperature, and washed again in PBS. Coverslips
873 were mounted onto glass slides with Vectashield mounting media containing DAPI (Vector Labs,
874 H-1200-10), sealed with nail polish, and imaged on a BZ-X800 microscope (Keyence) with a
875 Nikon S Plan Fluor ELWD ADM 40XC/0.60NA dry/oil objective and a 2/3-inch, 2.83 million
876 pixel Peltier-cooled monochrome CCD (colorized with LC filter) camera, supporter by the BZ-
877 X800 analyzer software. Images of astrocytes were acquired in red, green, and/or DAPI channels
878 using a CCD camera. Astrocytes that contained a single nucleus as revealed by DAPI stain,
879 strongly expressed fluorescent markers, and did not overlap with other labeled astrocytes were
880 selected for imaging (https://www.protocols.io/view/immunocytochemistry-14egn2556g5d/v1).

881 Astrocyte branch number and mitochondrial localization were analyzed using Seg_Astro
882 MATLAB (RRID: SCR_001622, version R2022b, http://www.mathworks.com/products/matlab/)
883 plugin. To quantify branch and mitochondrial number and size across the astrocyte arbor,
884 Seg_Astro (https://github.com/Eroglu-Lab/seg_cul_astro_app/tree/main) first detects the
885 astrocyte as well as the mitochondria by identifying locally significant regions based on order
886 statistics(Wang et al., 2020). Specifically, for the detection of the astrocyte, due to the nonuniform
887 intensity inside the cell, the initial detection contained many fragments. We further refined the
888 detection by searching for the globally optimal linkage, which is based on the graph design that
889 each node represents a fragment and the edge weight between nodes represents the mean intensity
890 of the brightest path between each pair of fragments. Then, the optimal linkage was obtained by
891 finding the min-spanning tree of the graph. Once the astrocyte is detected, Seg_Astro then uses
892 branch width and branchpoints to determine the astrocyte branch hierarchy and assign four types
893 of astrocyte branches per cell: 1) soma and primary processes, 2) secondary processes, 3) fine
894 processes, and 4) the terminal tips of processes (Fig. 2C). Seg_Astro then bins mitochondria into
895 these 4 branch types and outputs branch number, mitochondrial number, and mitochondrial size
896 per branch type. Importantly, we excluded mitochondrial measurements from the soma and
897 primary branches of astrocytes as mitochondria form a dense network in these compartments that
898 cannot be distinguished as discrete mitochondria for number and size quantification. Image
899 acquisition and analysis were performed blinded to experimental conditions. Each independent
900 experiment consisted of primary neurons and astrocytes isolated from a unique litter of wild-type

901 rats of mixed sexes. The exact number of independent experiments and the exact number of cells
902 analyzed are indicated in the figure legend for each experiment. Branch and mitochondrial number
903 per conditions were statistically analyzed using nested t-test or nested one-way ANOVA on
904 Graphpad Prism 9.

905 **Postnatal Astrocyte Labeling by Electroporation (PALE)**

906 Late P0/early P1 mice were sedated by hypothermia until anesthetized and 1 μL of plasmid DNA
907 mixed with Fast Green Dye was injected into the lateral ventricle of one hemisphere using a pulled
908 glass pipette. For mCherryCAAX labeling and shRNA knockdown experiments in pups from mito-
909 EGFP mice crossed with wild-type CD1 mice, the 1 μL of DNA contained 0.8 μg of pGLAST-
910 PBase, 0.7 μg of pPB-shRNA-mCherryCAAX, and 0.5 μg of pCAG-Cre (RRID:
911 Addgene_13775). Following DNA injection, electrodes were oriented with the positive terminal
912 above the visual cortex and the negative terminal below the chin, and 5 discrete 50 msec pulses of
913 100 V spaced 950 msec apart were applied. Pups were recovered on a heating pad, returned to their
914 home cage, and monitored until collection at P4, P7, P14, P21, P60, or P180. In the case of plasmid
915 expression in CD1 mice, assignment to experimental groups was randomly determined for each
916 litter. The number of replicates for each experiment is indicated in the figure legends. All animals
917 that appeared healthy at the time of collection were processed for data collection. All brain sections
918 were examined for the presence of electroporated cells before staining and downstream analyses
919 (https://dx.doi.org/10.17504/protocols.io.8epv5op66g1b/v1).

920 **Tamoxifen administration**

921 Tamoxifen (Sigma, T5648) was dissolved in corn oil (Sigma, 8267) at a concentration of 10 mg/mL
922 and further diluted in corn oil to 1.25 mg/mL. 40 μL of the tamoxifen solution was injected into
923 the milk spot using an insulin syringe, for a dose of 0.05 mg at P1, P2, and P3. Two tamoxifen
924 injections (P1 and P2) were sufficient turn on tdTomato expression in all astrocytes, however a
925 third dose of tamoxifen (at P3) was needed for achieving a significant decrease of Drp1 levels in
926 astrocytes (https://dx.doi.org/10.17504/protocols.io.dm6gp21b5lzp/v1).

927 **EdU administration**

928 EdU stock solution from Click-iT EdU Imaging Kit (Thermofisher, C10640) was diluted in DPBS
929 to a concentration of 10μM (2.5μg of EdU/μl). At timepoints noted in Supplemental Figure 4, pups
930 were weighed and injected with 15μg of EdU per gram of animal weight (6μl of working 10μM
931 EdU stock solution per gram of animal weight). Animals were collected for staining 16 hours after
932 EdU injection and tissue sections were stained following the Click-iT EdU Imaging Kit
933 manufacturer protocol (https://dx.doi.org/10.17504/protocols.io.8epv5m5bdl1b/v1).

934 **Immunohistochemistry**

935 *Sample Preparation* Mice used for immunohistochemistry were anesthetized with 200 mg/kg
936 tribromoethanol (avertin) and perfused with TBS/Heparin and 4% PFA. Brains were collected and
937 post-fixed in 4% PFA overnight, cryoprotected in 30% sucrose, frozen in a solution containing 2
938 parts 30% sucrose and 1 part TissueTek O.C.T. (Sakura Finetek, cat#4583) and stored at −80°C.
939 Floating coronal tissue sections of 30, 40, 100 μm thickness were collected and stored in a 1:1
940 mixture of TBS/glycerol at −20°C. For immunostaining, sections were washed in 1x TBS
941 containing 0.2% Triton-X 100 (TBST), blocked in 10% NGS diluted in TBST, and incubated in
942 primary antibody for 2-3 nights at 4°C with shaking. Primary antibodies used were: anti-RFP
943 (Rabbit, 1:2000, RRID:AB_2209751), GFP (Chicken, 1:2000, RRID:AB_10000240), Sox9
944 (Rabbit, 1:2000, RRID:AB_2239761), Connexin43 (Rabbit, 1:100, RRID:AB_2294590), Drp1
945 (Mouse, 1:100, RRID:AB_398424), Connexin30 (Rabbit, 1:500, RRID:AB_2533979), and GFAP
946 (Rabbit, 1:1000, RID:AB_10013382). Following primary incubation, sections were washed in
947 TBST, incubated in Alexa-Fluor conjugated secondary antibodies diluted 1:200 (Life
948 Technologies) for 2-3 hours at room temperature, washed with TBST, and mounted onto glass
949 slides using a homemade mounting media (90% Glycerol, 20 mM Tris pH 8.0, 0.5% n-Propyl
950 gallate) and sealed with nail polish. For primary antibodies produced in mouse, isotype specific
951 secondary antibodies were always used (e.g. goat anti-mouse IgG1) to avoid excessive background
952 staining. For DAPI staining, DAPI (1:50,000) was added to the secondary antibody solution for
953 the final 10 minutes of incubation. (https://dx.doi.org/10.17504/protocols.io.261ge876og47/v1).

954 *Astrocyte territory volume analysis* To assess the territory volume of individual astrocytes in the
955 developing mouse cortex, 100 μm-thick floating sections containing V1 astrocytes labeled sparsely
956 via PALE with mCherry-CAAX and mito-EGFP were collected. In shDrp1 conditions where

957 astrocytes cluster together, only single astrocytes on the periphery of clusters were used for this
958 analysis. Images containing an entire astrocyte (50-60 µm Z-stack) were acquired at 21°C on an
959 Olympus FV 3000 microscope with an Olympus Plan APO 60× 1.4 NA oil objective (Immoil-
960 f30cc), supported by the Olympus FV315-SW software. Criteria for data inclusion required that
961 the entirety of the astrocyte could be captured within a single brain section, and that the astrocyte
962 was located in layers 2/3, 4, or 5 of the visual cortex. Astrocytes in which the entire astrocyte could
963 not be captured within the section or were located in other layers or outside of the visual cortex
964 were excluded from the study and not imaged. Imaged astrocytes were analyzed using Imaris
965 Bitplane software (RRID: SCR_007370, version 9.9.9, https://imaris.oxinst.com/packages) as
966 described previously (Stogsdill et al., 2017). Briefly, surface reconstructions were generated and
967 the Imaris Xtensions "Visualize Surface Spots" and "Convex Hull" were used to create an
968 additional surface render representing the territory of the astrocyte. The volume of each territory
969 was recorded, and astrocyte territory sizes from biological replicates were analyzed across
970 experimental conditions using a nested t-test. The number of mice and cells/mouse analyzed are
971 specified in the figure legend for each experiment.

972 *Neuropil infiltration volume analysis* To measure the extent of astrocyte infiltration into the
973 neuropil, astrocyte images were acquired from mCherry-CAAX and mito-EGFP labeled astrocytes
974 in 40 µm brain sections. Images were acquired at 21°C on an Olympus FV3000 microscope with
975 an Olympus Plan APO 60× 1.4 NA oil objective (Immoil-f30cc) and a 2x zoom, supported by the
976 Olympus FV315-SW software. Criteria for inclusion required the astrocyte to be located within
977 layer 2/3, 4, or 5 of the visual cortex, express the fluorescent label, include their soma in the z-
978 stack capture, and have at least 15µm in the z-dimension contained within the section. Astrocytes
979 that did not meet these criteria were excluded from the study and not imaged. For each astrocyte,
980 three ROIs (12.65 µm x 12.65 µm x 10 µm) containing the neuropil, and devoid of cell soma, large
981 branches, and end feet were chosen and reconstructed using the surface tool in Imaris. The surface
982 volume of each ROI was calculated and the three data points from each astrocyte were averaged.
983 Data from biological replicates were analyzed using a nested t-test. The number of mice and
984 cells/mouse analyzed are specified in the figure legend for each experiment.

985 *Mitochondrial average volume, number, and total volume analysis* To measure mitochondrial size
986 (average volume), number, and total volume within whole astrocytes or distal astrocyte process,

987 astrocyte images were captured as described above in *Astrocyte territory volume analysis* (for
988 whole astrocyte mitochondrial volume) or *Neuropil infiltration volume analysis* (for distal NIV
989 mitochondrial volume). In Imaris, the astrocyte volume rendered above was used to mask the
990 mitochondrial EGFP channel. Either whole or distal mitochondria were reconstructed using the
991 surface volume tool in Imaris (Surface detail: 0.1, Background subtraction: 0.5, Volume filter:
992 0.01). Data from biological replicates were analyzed using a nested t-test. The number of mice and
993 cells/mouse analyzed are specified in the figure legend for each experiment.

994 *Quantification of astrocyte cell or cluster area* To analyze astrocyte cell or cluster area of sparse
995 Drp1 knockdown PALE experiments, three 40µm sections per animal were imaged at 21°C on an
996 Olympus FV 3000 microscope with an Olympus UPlanSApo 10x/0.40 dry objective, supported by
997 the Olympus FV315-SW software and loaded into ImageJ. The astrocyte mCherry channel, the
998 RFP channel, was selected. The image was then stacked into a max projection z-stack and a
999 gaussian blur of sigma radius 1.00 was applied. A threshold was then applied to the image to
1000 include signal from astrocytes in the cortex above the subventricular zone. Then, using ImageJ
1001 analysis, the area of each cluster above 500 pixels per image was recorded. The average cluster
1002 area per image was calculated and 3 technical replicates per animal were averaged for analysis.
1003 Data from biological replicates were analyzed using a nested t-test. The number of mice and
1004 cells/mouse analyzed are specified in the figure legend for each experiment.

1005 *Nearest and multiple neighbor analysis* To measure the distance between astrocyte neighbors in
1006 sparse Drp1 knockdown PALE experiments, images of astrocytes or astrocyte clusters from 40µm
1007 sections were captured at 21°C on a Leica Stellaris 8 Confocal with a 63x/1.40 HC PL APO CS2
1008 (11506350) oil objective (Leica F Immersion liquid (Oil) 11513859) and a Leica K5 sCMOS
1009 (14402610) camera, supported by the Leica Application Suite X (LASX, build 4.5.0.25531)
1010 software and loaded into ImageJ. Composite images merging the DAPI channel for all nuclei, Sox9
1011 channel for astrocytic nuclei, and the RFP channel for astrocytes were generated. Using the line
1012 tool, a line was manually drawn from the edge of one Sox9+ nucleus within mCherry to the closest
1013 Sox9+ nucleus and the length of the line was measured. Each distance between neighbors was
1014 recorded from the same animal as technical replicates. Data from biological replicates were
1015 analyzed using a nested t-test. To quantify the number of Sox9+ nuclei, the composite images from
1016 above were used, and the number of Sox9+ nuclei within mCherry signal was manually counted.

1017 The number of Sox9+ nuclei per cell or cluster were recorded as technical replicates per mouse.
1018 The number of mice and cells/mouse analyzed are specified in the figure legend for each
1019 experiment. In the Drp1 conditional deletion mouse model, V1 cortical images of 30µm sections
1020 were taken at 21°C on a Leica Stellaris 8 Confocal with a 20x/0.75 HC PL APO CS2 (11506343)
1021 immersion objective (Leica F Immersion liquid (Oil) 11513859) at 0.75 optical zoom and a Leica
1022 K5 sCMOS (14402610) camera, supported by the Leica Application Suite X (LASX, build
1023 4.5.0.25531) software. Single optical section images were loaded onto Imaris with a z-size of 0.01
1024 µm. Selecting the tdTomato channel, soma spots were generated with an estimated XY diameter
1025 of 7.5 µm and with background subtraction using Imaris Spots tool. Object-Object statistics were
1026 collected for the spots generated. Once these soma spots were generated, distance to nearest
1027 neighbor and average distance to 9 neighbors were analyzed. Data from biological replicates were
1028 analyzed using a nested t-test and Kolmogorov-Smirnov test. The number of mice and cells/mouse
1029 analyzed are specified in the figure legend for each experiment.

1030 *Aldh1l1-Drp1 mouse model recombination efficiency analysis with Sox9* In the Drp1 conditional
1031 deletion mouse model, V1 cortical images of 30µm sections were taken at 21°C on a Leica Stellaris
1032 8 Confocal with a 20x/0.75 HC PL APO CS2 (11506343) immersion objective (Leica F Immersion
1033 liquid (Oil) 11513859) at 0.75 optical zoom and a Leica K5 sCMOS (14402610) camera, supported
1034 by the Leica Application Suite X (LASX, build 4.5.0.25531) software. A z-stack of 5µm with a
1035 step size of 1 µm was captured. Images were loaded onto Imaris and the surface tool was used to
1036 create a mask of the tdTomato channel. This tdTomato mask was used to sort Sox9+ signal within
1037 tdTomato and outside tdTomato separately. Soma spots for Sox9+ nuclei within and outside of
1038 tdTomato were generated with an estimated XY diameter of 6 µm and with background subtraction
1039 using Imaris Spots tool. Once these spots were generated, the number of Sox9+ spots were
1040 collected for both inside and outside tdTomato signal. Total number of Sox9+ spots were calculated
1041 as the sum of Sox9+ spots inside and outside tdTomato. The percent recombination efficiency was
1042 quantified was the number of Sox9+ spots within tdTomato signal divided by total Sox9+ spots
1043 per field of view. The number of mice and cells/mouse analyzed are specified in the figure legend
1044 for each experiment.

1045 *Connexin43 volume analysis* To quantify the amount of Connexin43 within astrocytes in the sparse
1046 Drp1 knockdown PALE model, images (0.5 µm z-step, 10 µm z-stacks) from 40µm sections of

1047 astrocytes or clusters were taken at 21°C on a Leica Stellaris 8 Confocal with a 93x/1.30 HC PL
1048 APO CS2 (11506417) glycerol objective (Leica G Immersion liquid (Glycerol) 11513910) and a
1049 Leica K5 sCMOS (14402610) camera, supported by the Leica Application Suite X (LASX, build
1050 4.5.0.25531) software. Criteria for inclusion required the astrocyte to be located within layer 2/3,
1051 4, and 5 of the visual cortex, express the fluorescent label, and have at least 10µm in the z-
1052 dimension contained within the section. For each astrocyte or astrocyte cluster, the Imaris surface
1053 tool was used to render the astrocyte volume. This astrocyte volume was then used to mask the
1054 Cx43 channel, and then Imaris surface tool was used to generate surface volumes of Cx43 puncta
1055 within the astrocyte volume territory only (Surface detail: 0.1, Background subtraction: 0.5,
1056 Volume filter: 0.01). Data from biological replicates were analyzed using a nested one-way
1057 ANOVA. The number of mice and cells/mouse analyzed are specified in the figure legend for each
1058 experiment.

1059 *Astrocyte density analysis* For quantifying the density of astrocytes in the Drp1 conditional
1060 deletion model, V1 cortical images of 30µm sections were taken at 21°C on a Leica Stellaris 8
1061 Confocal with a 20x/0.75 HC PL APO CS2 (11506343) immersion objective (Leica F Immersion
1062 liquid (Oil) 11513859) at 0.75 optical zoom and a Leica K5 sCMOS (14402610) camera, supported
1063 by the Leica Application Suite X (LASX, build 4.5.0.25531) software. Using the tdTomato channel
1064 on ImageJ, a rectangular region of interest (ROI) that encompassed all cortical layers of the visual
1065 cortex was selected and saved to the ROI manager in ImageJ. Within the multi-layer rectangular
1066 ROI, ROIs for each cortical layer were drawn and saved. The area of each ROI was recorded.
1067 These imaging parameters and ROIs were also used for the *Cortical Astrocyte coverage analysis*
1068 and *Drp1 protein expression analyses by immunohistochemistry* below. The 'Show-all' feature on
1069 the ROI manager was selected, so that the boundaries between cortical layers were shown. Using
1070 the Cell Counter plug-in (RRID:SCR_025376, https://imagej.net/ij/plugins/cell-counter.html),
1071 tdTomato+ somas were manually counted. The number of somas across the cortex was calculated
1072 as the sum of tdTomato+ somas in all cortical layers. Density of tdTomato+ somas was calculated
1073 by dividing the number of tdTomato+ somas by their corresponding ROI area. GFAP+ cell density
1074 was calculated and analyzed in the same manner, using the GFAP channel instead of the tdTomato
1075 channel. Three sections were analyzed as technical replicates per mouse. Data from biological

1076 replicates were analyzed using a two-way ANOVA with Sidak's multiple comparisons test. The
1077 number of mice and cells/mouse analyzed are specified in the figure legend for each experiment.

1078 *Cortical Astrocyte coverage analysis* To quantify astrocyte coverage across the cortex in the Drp1
1079 conditional deletion model, cortical images were captured and divided into multiple ROIs for
1080 analysis as described above in *Astrocyte density analysis*. Using the threshold tool in ImageJ, the
1081 tdTomato channel coverage was binarized and saved as a tdTomato mask. Then, selecting each
1082 cortical ROI, the area of tdTomato coverage from the mask generated across the cortex and per
1083 layer was collected. tdTomato coverage was defined as the percent of tdTomato+ area divided by
1084 the density of tdTomato+ cells. GFAP coverage was calculated and analyzed in the same manner,
1085 using the GFAP channel instead of the tdTomato channel. GFAP coverage likewise normalized by
1086 tdTomato density. Three sections were analyzed as technical replicates per mouse. Data from
1087 biological replicates were analyzed using a two-way ANOVA with Sidak's multiple comparisons
1088 test. The number of mice and cells/mouse analyzed are specified in the figure legend for each
1089 experiment.

1090 *Drp1 protein expression analyses by immunohistochemistry* For quantifying Drp1 protein levels
1091 in the Drp1 conditional deletion model, cortical images were captured and divided into multiple
1092 ROIs for analysis as described above in *Astrocyte density analysis*. Then a mask of the tdTomato
1093 channel was applied to the Drp1 channel and mean gray value of Drp1 within astrocytes was
1094 collected per layer and across the cortex using ImageJ. The collected values were normalized to
1095 tdTomato+ soma density. Three sections were analyzed as technical replicates per mouse. Data
1096 from biological replicates were analyzed using a two-way ANOVA with Sidak's multiple
1097 comparisons test. The number of mice and cells/mouse analyzed are specified in the figure legend
1098 for each experiment.

1099 *Cx43 protein expression analysis by immunohistochemistry* To measure Cx43 protein levels in
1100 astrocytes in the Drp1 conditional deletion model, cortical images were captured as described
1101 above in *Astrocyte density analysis*. ImageJ was used to subtract background from the Cx43
1102 channel with a rolling ball radius of 50 units. Following background subtraction, individual
1103 astrocytes within layers 2/3, 4, or 5 were outlined with the freehand tool using tdTomato to
1104 determine astrocyte territories, and astrocyte outlines were saved as ROIs. Astrocyte ROIs were

applied to Cx43 channel and the mean gray value of Cx43 signal was collected per astrocyte and normalized by the ROI area. Three sections were analyzed as technical replicates per mouse. Data from biological replicates were analyzed using a nested t-test, Kolmogorov-Smirnov test. The number of mice and cells/mouse analyzed are specified in the figure legend for each experiment.

Cortical thickness analysis: To measure cortical thickness in Drp1 cWT and cKO mice, images of V1 cortices were taken on at 21°C on a Leica Stellaris 8 Confocal with a 10x/0.40 HC PL APO CS2 (11506424) dry objective and a Leica K5 sCMOS (14402610) camera, supported by the Leica Application Suite X (LASX, build 4.5.0.25531) software. Images were loaded into ImageJ and the line tool was used to record length. Three lines per section were drawn from the subventricular zone to the Pia. The lengths of these lines were averaged per section for 3 sections per mouse, and data from each section was plotted as a technical replicate per mouse. Data from biological replicates were analyzed using a nested t-test.

Quantification and statistical analysis

All statistical analyses were performed using Graphpad Prism (RRID: SCR_002798, version 9, https://www.graphpad.com/scientific-software/prism/). The exact number of replicates, specific statistical tests, and P values for each experiment are indicated in the figures and figure legends. All data are represented as mean ± SEM, and individual data points are shown for all data, where applicable. Where indicated, nested t-tests were applied with an alpha threshold of 0.05 for adjusted P-value. A Geisser-Greenhouse correction was used for both One-way and Two-way ANOVA analyses. All experimental animals that appeared healthy at the time of tissue collection were processed for data collection. Specific details for inclusion, exclusion, and randomization are included in the specific subsections of the Materials and methods details section.

Online supplemental material

Fig. S1 contains qPCR validation of shRNAs targeting mouse and rat Drp1, mouse Mfn1, and mouse Miro 1. Fig. S2 emphasizes how silencing astrocytic mitochondrial dynamics modifies mitochondrial numbers and size. Fig. S3 establishes Drp1 KD astrocyte clusters are not a result of increased astrocyte proliferation, persist into adulthood, and express gap-junction protein Cx30. Fig. S4 characterizes the astrocyte-specific Drp1 cKO model, demonstrating decreased Drp1

1133 protein expression, Cre-mediated recombination efficiency, and additional astrocyte reactivity
1134 markers probed in isolated astrocytes from Drp1 cKO and cWT mice.

1135

ACKNOWLEDGMENTS

We thank Drs. Romain Cartoni and Chantell Evans for critical feedback on this manuscript. We thank Sarah Johnson and Donna Porter for their excellent technical help. This work was supported by a Paul and Daisy Soros Fellowship (2020) and an HHMI Gilliam Fellowship (GT15076) to MPRS, a Chan Zuckerberg Initiative Neurodegeneration Challenge Network Collaborative grant (DAF2018-191999 and DAF2021-237435) to CE, an N.I.H. grant U19-NS123719 to CE and GY, and by the joint efforts of MJFF and the Aligning Science Across Parkinson's (ASAP) initiative. MJFF administers the grant ASAP-020607 to CE for ASAP and the Michael J Fox Foundation. Dr. Cagla Eroglu is an HHMI Investigator.

IP RIGHTS NOTICE

This article is subject to HHMI's Open Access to Publications policy. HHMI lab heads have previously granted a nonexclusive CC BY 4.0 license to the public and a sublicensable license to HHMI in their research articles. Pursuant to those licenses, the author-accepted manuscript of this article can be made freely available under a CC BY 4.0 license immediately upon publication.

CONFLICT OF INTEREST STATEMENT

The authors declare no competing financial interests.

AUTHOR CONTRIBUTIONS

Conceptualization, Maria Pia Rodriguez Salazar (MPRS) and Cagla Eroglu (CE); Data Curation, MPRS, Sprihaa Kolanukuduru (SK), Valentina Ramirez (VR); Formal analysis, MPR, SK, VR; Funding Acquisition, MPRS, Guoqiang Yu (GY), CE; Investigation, MPRS, SK, VR, Gracie Manigault (GM), Gabrielle Sejourne (GS); Methodology, MPRS, SK, VR, Boyu Lyu (BL); Project Administration, MPRS, CE; Resources, MPRS, BL, GY, Hiromi Sesaki (HS); Software, MPRS, BL, VR; Supervision, MPRS, CE; Validation, MPRS, SK, VR; Visualization, MPRS, SK, VR, CE; Writing – original draft, MPRS, SK, VR, CE; Writing – Review & Editing, MPRS, SK, VR, BL, GM, GS, HS, GY, CE;.

REFERENCES

Abati, E., A. Manini, D. Velardo, R. Del Bo, L. Napoli, F. Rizzo, M. Moggio, N. Bresolin, E. Bellone, M.T. Bassi, M.G. D'Angelo, G.P. Comi, and S. Corti. 2022. Clinical and genetic features of a cohort of patients with MFN2-related neuropathy. *Scientific Reports*. 12:6181.

Agarwal, A., P.H. Wu, E.G. Hughes, M. Fukaya, M.A. Tischfield, A.J. Langseth, D. Wirtz, and D.E. Bergles. 2017. Transient Opening of the Mitochondrial Permeability Transition Pore Induces Microdomain Calcium Transients in Astrocyte Processes. *Neuron*. 93:587-605.e587.

Allen, N.J., and D.A. Lyons. 2018. Glia as architects of central nervous system formation and function. *Science*. 362:181-185.

Alvarez, J.I., T. Katayama, and A. Prat. 2013. Glial influence on the blood brain barrier. *Glia*. 61:1939-1958.

Baldwin, K.T., C.X. Tan, S.T. Strader, C. Jiang, J.T. Savage, X. Elorza-Vidal, X. Contreras, T. Rülicke, S. Hippenmeyer, R. Estévez, R.R. Ji, and C. Eroglu. 2021. HepaCAM controls astrocyte self-organization and coupling. *Neuron*. 109:2427-2442.e2410.

Billups, B., and I.D. Forsythe. 2002. Presynaptic Mitochondrial Calcium Sequestration Influences Transmission at Mammalian Central Synapses. *The Journal of Neuroscience*. 22:5840.

Bushong, E.A., M.E. Martone, and M.H. Ellisman. 2004. Maturation of astrocyte morphology and the establishment of astrocyte domains during postnatal hippocampal development. *International Journal of Developmental Neuroscience*. 22:73-86.

Bushong, E.A., M.E. Martone, Y.Z. Jones, and M.H. Ellisman. 2002. Protoplasmic astrocytes in CA1 stratum radiatum occupy separate anatomical domains. *J Neurosci*. 22:183-192.

Casillas-Espinosa, P.M., K.L. Powell, and T.J. O'Brien. 2012. Regulators of synaptic transmission: roles in the pathogenesis and treatment of epilepsy. *Epilepsia*. 53 Suppl 9:41-58.

Cassina, P., E. Miquel, L. Martínez-Palma, and A. Cassina. 2025. Mitochondria and astrocyte reactivity: Key mechanism behind neuronal injury. *Neuroscience*. 567:227-234.

Chen, F., and J. LoTurco. 2012. A method for stable transgenesis of radial glia lineage in rat neocortex by piggyBac mediated transposition. *J Neurosci Methods*. 207:172-180.

Chen, H., S.A. Detmer, A.J. Ewald, E.E. Griffin, S.E. Fraser, and D.C. Chan. 2003. Mitofusins Mfn1 and Mfn2 coordinately regulate mitochondrial fusion and are essential for embryonic development. *J Cell Biol*. 160:189-200.

Cheung, G., O. Chever, A. Rollenhagen, N. Quenech'du, P. Ezan, J.H.R. Lübke, and N. Rouach. 2023. Astroglial Connexin 43 Regulates Synaptic Vesicle Release at Hippocampal Synapses. *Cells*. 12.

Chih, B., L. Gollan, and P. Scheiffele. 2006. Alternative splicing controls selective trans-synaptic interactions of the neuroligin-neurexin complex. *Neuron*. 51:171-178.

Chung, W.S., N.J. Allen, and C. Eroglu. 2015. Astrocytes Control Synapse Formation, Function, and Elimination. *Cold Spring Harb Perspect Biol*. 7:a020370.

Clasadonte, J., E. Scemes, Z. Wang, D. Boison, and P.G. Haydon. 2017. Connexin 43-Mediated Astroglial Metabolic Networks Contribute to the Regulation of the Sleep-Wake Cycle. *Neuron*. 95:1365-1380.e1365.

Clavreul, S., L. Abdeladim, E. Hernández-Garzón, D. Niculescu, J. Durand, S.-H. Ieng, R. Barry, G. Bonvento, E. Beaurepaire, J. Livet, and K. Loulier. 2019. Cortical astrocytes develop in a plastic manner at both clonal and cellular levels. *Nature Communications*. 10:4884.

Courchet, J., T.L. Lewis, Jr., S. Lee, V. Courchet, D.Y. Liou, S. Aizawa, and F. Polleux. 2013. Terminal axon branching is regulated by the LKB1-NUAK1 kinase pathway via presynaptic mitochondrial capture. *Cell*. 153:1510-1525.

1208 Cunniff, B., A.J. McKenzie, N.H. Heintz, and A.K. Howe. 2016. AMPK activity regulates trafficking of
1209 mitochondria to the leading edge during cell migration and matrix invasion. *Molecular biology*
1210 *of the cell*. 27:2662-2674.
1211 da Silva, A.F., F.R. Mariotti, V. Máximo, and S. Campello. 2014. Mitochondria dynamism: of shape,
1212 transport and cell migration. *Cell Mol Life Sci*. 71:2313-2324.
1213 Dermietzel, R., E.L. Hertberg, J.A. Kessler, and D.C. Spray. 1991. Gap junctions between cultured
1214 astrocytes: immunocytochemical, molecular, and electrophysiological analysis. *J Neurosci*.
1215 11:1421-1432.
1216 Fahrner, J.A., R. Liu, M.S. Perry, J. Klein, and D.C. Chan. 2016. A novel de novo dominant negative
1217 mutation in DNM1L impairs mitochondrial fission and presents as childhood epileptic
1218 encephalopathy. *Am J Med Genet A*. 170:2002-2011.
1219 Fiebig, C., S. Keiner, B. Ebert, I. Schäffner, R. Jagasia, D.C. Lie, and R. Beckervordersandforth. 2019.
1220 Mitochondrial Dysfunction in Astrocytes Impairs the Generation of Reactive Astrocytes and
1221 Enhances Neuronal Cell Death in the Cortex Upon Photothrombotic Lesion. *Frontiers in*
1222 *molecular neuroscience*. 12:40-40.
1223 Fransson, Å., A. Ruusala, and P. Aspenström. 2006. The atypical Rho GTPases Miro-1 and Miro-2 have
1224 essential roles in mitochondrial trafficking. *Biochemical and biophysical research*
1225 *communications*. 344:500-510.
1226 Friedman, J.R., and J. Nunnari. 2014. Mitochondrial form and function. *Nature*. 505:335-343.
1227 Giaume, C., A. Koulakoff, L. Roux, D. Holcman, and N. Rouach. 2010. Astroglial networks: a step
1228 further in neuroglial and gliovascular interactions. *Nat Rev Neurosci*. 11:87-99.
1229 Gollihue, J.L., and C.M. Norris. 2020. Astrocyte mitochondria: Central players and potential
1230 therapeutic targets for neurodegenerative diseases and injury. *Ageing Res Rev*. 59:101039.
1231 Gu, X., W. Chen, Z. Li, X. Wang, Q. Su, and F. Zhou. 2025. Drp1 mitochondrial fission in astrocyte
1232 modulates behavior and neuroinflammation during morphine addiction. *Journal of*
1233 *Neuroinflammation*. 22:108.
1234 Göbel, J., P. Pelzer, E. Engelhardt, V. Sakthivelu, H.M. Jahn, M. Jevtic, K. Folz-Donahue, C. Kukat, A.
1235 Schauss, C.K. Frese, A. Ghanem, K.-K. Conzelmann, E. Motori, and M. Bergami. 2019.
1236 Mitochondrial fusion in reactive astrocytes coordinates local metabolic domains to promote
1237 vascular repair. *bioRxiv*:657999.
1238 Haseleu, J., E. Anlauf, S. Blaess, E. Endl, and A. Derouiche. 2013. Studying subcellular detail in fixed
1239 astrocytes: dissociation of morphologically intact glial cells (DIMIGs). *Frontiers in Cellular*
1240 *Neuroscience*. 7.
1241 Holt, L.M., R.D. Hernandez, N.L. Pacheco, B. Torres Ceja, M. Hossain, and M.L. Olsen. 2019.
1242 Astrocyte morphogenesis is dependent on BDNF signaling via astrocytic TrkB.T1. *Elife*. 8.
1243 Homkajorn, B., N.R. Sims, and H. Muyderman. 2010. Connexin 43 regulates astrocytic migration and
1244 proliferation in response to injury. *Neurosci Lett*. 486:197-201.
1245 Hösli, L., N. Binini, K.D. Ferrari, L. Thieren, Z.J. Looser, M. Zuend, H.S. Zanker, S. Berry, M. Holub, W.
1246 Möbius, T. Ruhwedel, K.A. Nave, C. Giaume, B. Weber, and A.S. Saab. 2022. Decoupling
1247 astrocytes in adult mice impairs synaptic plasticity and spatial learning. *Cell Rep*. 38:110484.
1248 Ignatenko, O., D. Chilov, I. Paetau, E. de Miguel, C.B. Jackson, G. Capin, A. Paetau, M. Terzioglu, L.
1249 Euro, and A. Suomalainen. 2018. Loss of mtDNA activates astrocytes and leads to spongiotic
1250 encephalopathy. *Nature Communications*. 9:70.
1251 Ishihara, N., M. Nomura, A. Jofuku, H. Kato, S.O. Suzuki, K. Masuda, H. Otera, Y. Nakanishi, I. Nonaka,
1252 Y.-i. Goto, N. Taguchi, H. Morinaga, M. Maeda, R. Takayanagi, S. Yokota, and K. Mihara. 2009.
1253 Mitochondrial fission factor Drp1 is essential for embryonic development and synapse
1254 formation in mice. *Nature Cell Biology*. 11:958-966.

1255 Kameritsch, P., K. Pogoda, and U. Pohl. 2012. Channel-independent influence of connexin 43 on cell
1256 migration. *Biochim Biophys Acta*. 1818:1993-2001.
1257 Ke, P., J. Gu, J. Liu, Y. Liu, X. Tian, Y. Ma, Y. Meng, and F. Xiao. 2023. Syntabulin regulates neuronal
1258 excitation/inhibition balance and epileptic seizures by transporting syntaxin 1B. *Cell Death*
1259 *Discov*. 9:187.
1260 Kim, H.J., M.R. Shaker, B. Cho, H.M. Cho, H. Kim, J.Y. Kim, and W. Sun. 2015. Dynamin-related protein
1261 1 controls the migration and neuronal differentiation of subventricular zone-derived neural
1262 progenitor cells. *Scientific Reports*. 5:15962.
1263 König, T., H. Nolte, M.J. Aaltonen, T. Tatsuta, M. Krols, T. Stroh, T. Langer, and H.M. McBride. 2021.
1264 MIROs and DRP1 drive mitochondrial-derived vesicle biogenesis and promote quality
1265 control. *Nat Cell Biol*. 23:1271-1286.
1266 Lagos-Cabré, R., F. Burgos-Bravo, A.M. Avalos, and L. Leyton. 2019. Connexins in Astrocyte
1267 Migration. *Front Pharmacol*. 10:1546.
1268 Lhuissier, C., B.E. Wagner, A. Vincent, G. Garraux, O. Hougrand, R. Van Coster, V. Benoit, D.
1269 Karadurmus, G. Lenaers, N. Gueguen, A. Chevrollier, and I. Maystadt. 2022. Case report:
1270 Thirty-year progression of an EMPF1 encephalopathy due to defective mitochondrial and
1271 peroxisomal fission caused by a novel de novo heterozygous DNM1L variant. *Front Neurol*.
1272 13:937885.
1273 Liu, X., Z. Zhang, D. Li, M. Lei, Q. Li, and P. Zhang. 2021. DNM1L-Related Mitochondrial Fission
1274 Defects Presenting as Encephalopathy: A Case Report and Literature Review. *Front Pediatr*.
1275 9:626657.
1276 Lovatt, D., U. Sonnewald, H.S. Waagepetersen, A. Schousboe, W. He, J.H.C. Lin, X. Han, T. Takano, S.
1277 Wang, F.J. Sim, S.A. Goldman, and M. Nedergaard. 2007. The Transcriptome and Metabolic
1278 Gene Signature of Protoplasmic Astrocytes in the Adult Murine Cortex. *The Journal of*
1279 *Neuroscience*. 27:12255.
1280 López-Doménech, G., and J.T. Kittler. 2023. Mitochondrial regulation of local supply of energy in
1281 neurons. *Curr Opin Neurobiol*. 81:102747.
1282 Middeldorp, J., and E.M. Hol. 2011. GFAP in health and disease. *Progress in Neurobiology*. 93:421-
1283 443.
1284 Moffat, J., D.A. Grueneberg, X. Yang, S.Y. Kim, A.M. Kloepfer, G. Hinkle, B. Piqani, T.M. Eisenhaure, B.
1285 Luo, J.K. Grenier, A.E. Carpenter, S.Y. Foo, S.A. Stewart, B.R. Stockwell, N. Hacohen, W.C.
1286 Hahn, E.S. Lander, D.M. Sabatini, and D.E. Root. 2006. A lentiviral RNAi library for human and
1287 mouse genes applied to an arrayed viral high-content screen. *Cell*. 124:1283-1298.
1288 Motori, E., J. Puyal, N. Toni, A. Ghanem, C. Angeloni, M. Malaguti, G. Cantelli-Forti, B. Berninger, K.-
1289 K. Conzelmann, M. Götz, Konstanze F. Winklhofer, S. Hrelia, and M. Bergami. 2013.
1290 Inflammation-Induced Alteration of Astrocyte Mitochondrial Dynamics Requires Autophagy
1291 for Mitochondrial Network Maintenance. *Cell Metabolism*. 18:844-859.
1292 Ni, H.M., J.A. Williams, and W.X. Ding. 2015. Mitochondrial dynamics and mitochondrial quality
1293 control. *Redox Biol*. 4:6-13.
1294 Oberheim, N.A., G.F. Tian, X. Han, W. Peng, T. Takano, B. Ransom, and M. Nedergaard. 2008. Loss of
1295 astrocytic domain organization in the epileptic brain. *J Neurosci*. 28:3264-3276.
1296 Pajarillo, E., A. Rizor, J. Lee, M. Aschner, and E. Lee. 2019. The role of astrocytic glutamate
1297 transporters GLT-1 and GLAST in neurological disorders: Potential targets for
1298 neurotherapeutics. *Neuropharmacology*. 161:107559.
1299 Paupe, V., and J. Prudent. 2018. New insights into the role of mitochondrial calcium homeostasis in
1300 cell migration. *Biochem Biophys Res Commun*. 500:75-86.

Pellerin, L., and P.J. Magistretti. 1994. Glutamate uptake into astrocytes stimulates aerobic glycolysis: a mechanism coupling neuronal activity to glucose utilization. *Proc Natl Acad Sci U S A*. 91:10625-10629.

Pellerin, L., G. Pellegri, P.G. Bittar, Y. Charnay, C. Bouras, J.L. Martin, N. Stella, and P.J. Magistretti. 1998. Evidence supporting the existence of an activity-dependent astrocyte-neuron lactate shuttle. *Dev Neurosci*. 20:291-299.

Popov, A., N. Brazhe, K. Morozova, K. Yashin, M. Bychkov, O. Nosova, O. Sutyagina, A. Brazhe, E. Parshina, L. Li, I. Medyanik, D.E. Korzhevskii, Z. Shenkarev, E. Lyukmanova, A. Verkhratsky, and A. Semyanov. 2023. Mitochondrial malfunction and atrophy of astrocytes in the aged human cerebral cortex. *Nature Communications*. 14:8380.

Rahman, M.H., and K. Suk. 2020. Mitochondrial Dynamics and Bioenergetic Alteration During Inflammatory Activation of Astrocytes. *Frontiers in Aging Neuroscience*. Volume 12 - 2020.

Rangaraju, V., M. Lauterbach, and E.M. Schuman. 2019. Spatially Stable Mitochondrial Compartments Fuel Local Translation during Plasticity. *Cell*. 176:73-84.e15.

Rash, J.E., T. Yasumura, F.E. Dudek, and J.I. Nagy. 2001. Cell-specific expression of connexins and evidence of restricted gap junctional coupling between glial cells and between neurons. *J Neurosci*. 21:1983-2000.

Reddy, P.H. 2014. Inhibitors of mitochondrial fission as a therapeutic strategy for diseases with oxidative stress and mitochondrial dysfunction. *J Alzheimers Dis*. 40:245-256.

Ren, D., P. Zheng, J. Feng, Y. Gong, Y. Wang, J. Duan, L. Zhao, J. Deng, H. Chen, S. Zou, T. Hong, and W. Chen. 2020. Overexpression of Astrocytes-Specific GJA1-20k Enhances the Viability and Recovery of the Neurons in a Rat Model of Traumatic Brain Injury. *ACS Chemical Neuroscience*. 11:1643-1650.

Shimura, D., E. Nuebel, R. Baum, S.E. Valdez, S. Xiao, J.S. Warren, J.A. Palatinus, T. Hong, J. Rutter, and R.M. Shaw. 2021. Protective mitochondrial fission induced by stress-responsive protein GJA1-20k. *Elife*. 10.

Smirnova, E., L. Griparic, D.L. Shurland, and A.M. van der Bliek. 2001. Dynamin-related protein Drp1 is required for mitochondrial division in mammalian cells. *Mol Biol Cell*. 12:2245-2256.

Smith, G.M., and G. Gallo. 2018. The role of mitochondria in axon development and regeneration. *Developmental neurobiology*. 78:221-237.

Smyth, J.W., and R.M. Shaw. 2013. Autoregulation of connexin43 gap junction formation by internally translated isoforms. *Cell Rep*. 5:611-618.

Srinivasan, R., T.Y. Lu, H. Chai, J. Xu, B.S. Huang, P. Golshani, G. Coppola, and B.S. Khakh. 2016. New Transgenic Mouse Lines for Selectively Targeting Astrocytes and Studying Calcium Signals in Astrocyte Processes In Situ and In Vivo. *Neuron*. 92:1181-1195.

Steketee, M.B., S.N. Moysidis, J.E. Weinstein, A. Kreymerman, J.P. Silva, S. Iqbal, and J.L. Goldberg. 2012. Mitochondrial dynamics regulate growth cone motility, guidance, and neurite growth rate in perinatal retinal ganglion cells in vitro. *Invest Ophthalmol Vis Sci*. 53:7402-7411.

Stephen, T.L., N.F. Higgs, D.F. Sheehan, S. Al Awabdh, G. Lopez-Domenech, I.L. Arancibia-Carcamo, and J.T. Kittler. 2015. Miro1 Regulates Activity-Driven Positioning of Mitochondria within Astrocytic Processes Apposed to Synapses to Regulate Intracellular Calcium Signaling. *J Neurosci*. 35:15996-16011.

Stogsdill, J.A., J. Ramirez, D. Liu, Y.-H. Kim, K.T. Baldwin, E. Enustun, T. Ejikeme, R.-R. Ji, and C. Eroglu. 2017. Astrocytic Neuroligins Control Astrocyte Morphogenesis and Synaptogenesis. *Nature*. 551:192-197.

Supplie, L.M., T. Düking, G. Campbell, F. Diaz, C.T. Moraes, M. Götz, B. Hamprecht, S. Boretius, D. Mahad, and K.-A. Nave. 2017. Respiration-Deficient Astrocytes Survive As Glycolytic Cells In Vivo. *The Journal of Neuroscience*. 37:4231.

Takano, T., J.T. Wallace, K.T. Baldwin, A.M. Purkey, A. Uezu, J.L. Courtland, E.J. Soderblom, T. Shimogori, P.F. Maness, C. Eroglu, and S.H. Soderling. 2020. Chemico-genetic discovery of astrocytic control of inhibition in vivo. *Nature*. 588:296-302.

Takumi, T., T. Ishii, Y. Horio, K.-I. Morishige, N. Takahashi, M. Yamada, T. Yamashita, H. Kiyama, K. Sohmiya, S. Nakanishi, and Y. Kurachi. 1995. A Novel ATP-dependent Inward Rectifier Potassium Channel Expressed Predominantly in Glial Cells *. *Journal of Biological Chemistry*. 270:16339-16346.

Tan, C.X., D.S. Bindu, E.J. Hardin, K. Sakers, R. Baumert, J.J. Ramirez, J.T. Savage, and C. Eroglu. 2023. δ-Catenin controls astrocyte morphogenesis via layer-specific astrocyte-neuron cadherin interactions. *J Cell Biol*. 222.

Vanstone, J.R., A.M. Smith, S. McBride, T. Naas, M. Holcik, G. Antoun, M.-E. Harper, J. Michaud, E. Sell, P. Chakraborty, M. Tetreault, J. Majewski, S. Baird, K.M. Boycott, D.A. Dyment, A. MacKenzie, M.A. Lines, and C. Care4Rare. 2016. DNM1L-related mitochondrial fission defect presenting as refractory epilepsy. *European Journal of Human Genetics*. 24:1084-1088.

Verkhratsky, A., R. Zorec, and V. Parpura. 2017. Stratification of astrocytes in healthy and diseased brain. *Brain Pathol*. 27:629-644.

Wakabayashi, J., Z. Zhang, N. Wakabayashi, Y. Tamura, M. Fukaya, T.W. Kensler, M. Iijima, and H. Sesaki. 2009a. The dynamin-related GTPase Drp1 is required for embryonic and brain development in mice. *J Cell Biol*. 186:805-816.

Wakabayashi, J., Z. Zhang, N. Wakabayashi, Y. Tamura, M. Fukaya, T.W. Kensler, M. Iijima, and H. Sesaki. 2009b. The dynamin-related GTPase Drp1 is required for embryonic and brain development in mice. *The Journal of cell biology*. 186:805-816.

Wang, Y., C. Wang, P. Ranefall, G.J. Broussard, G. Shi, B. Lyu, C.T. Wu, L. Tian, and G. Yu. 2020. SynQuant: an automatic tool to quantify synapses from microscopy images. *Bioinformatics*. 36:1599-1606.

Wiencken-Barger, A.E., B. Djukic, K.B. Casper, and K.D. McCarthy. 2007. A role for Connexin43 during neurodevelopment. *Glia*. 55:675-686.

Xiao, S., D. Shimura, R. Baum, D.M. Hernandez, S. Agvanian, Y. Nagaoka, M. Katsumata, P.D. Lampe, A.G. Kleber, T. Hong, and R.M. Shaw. 2020. Auxiliary trafficking subunit GJA1-20k protects connexin-43 from degradation and limits ventricular arrhythmias. *The Journal of Clinical Investigation*. 130:4858-4870.

Youle, R.J., and A.M. van der Bliek. 2012. Mitochondrial fission, fusion, and stress. *Science*. 337:1062-1065.

Zehnder, T., F. Petrelli, J. Romanos, E.C. De Oliveira Figueiredo, T.L. Lewis, Jr., N. Déglon, F. Polleux, M. Santello, and P. Bezzi. 2021. Mitochondrial biogenesis in developing astrocytes regulates astrocyte maturation and synapse formation. *Cell Rep*. 35:108952.

Zipursky, S., J. Lee, A. Sergeeva, G. Ahlsen, S. Mannepalli, F. Bahna, K. Goodman, B. Khakh, J. Weiner, L. Shapiro, and B. Honig. 2024. Astrocyte morphogenesis requires self-recognition. *Res Sq*.

Fig 1: Mitochondria increase in number and decrease in size during cortical astrocyte morphogenesis *in vivo.*

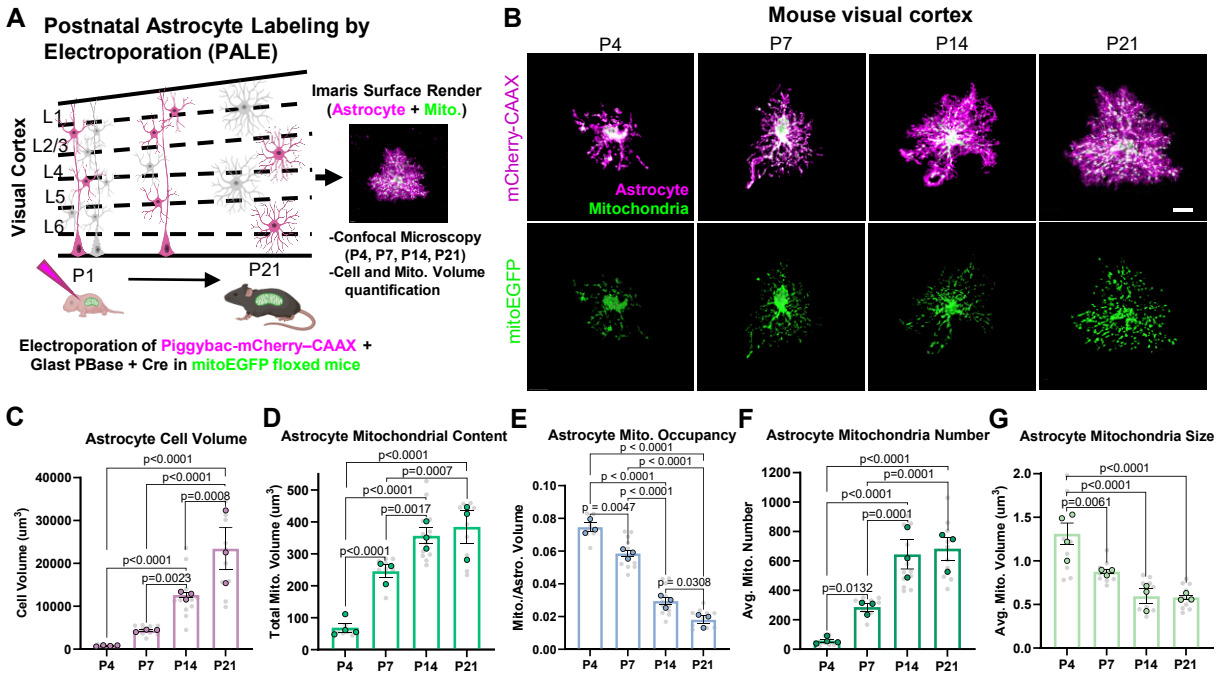

Fig 2: Mitochondrial occupy fine astrocyte processes concurrently with astrocyte morphological arborization *in vitro.*

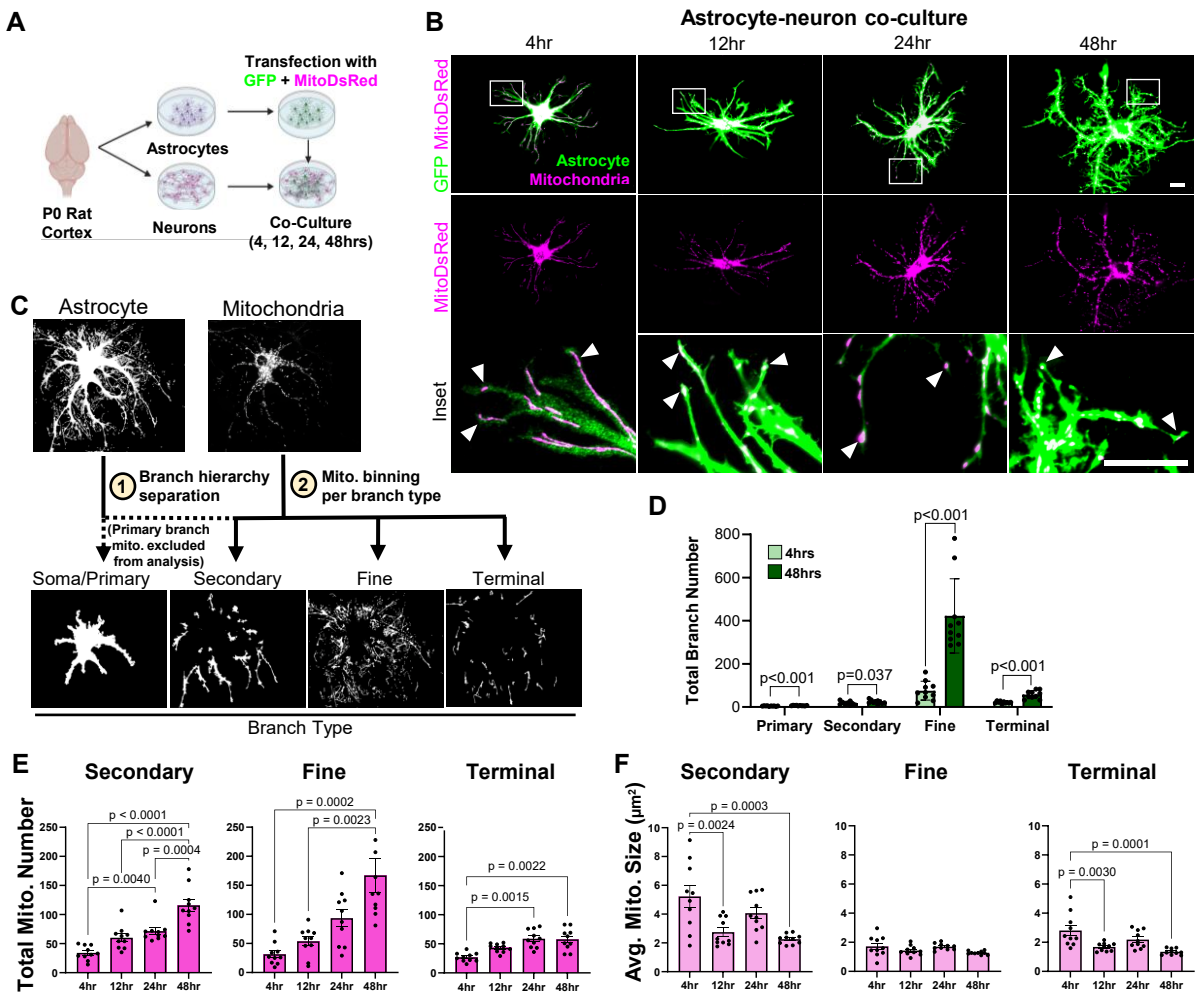

Fig 3: Drp1-induced mitochondrial fission is required for fine astrocyte process formation and mitochondrial localization *in vitro.*

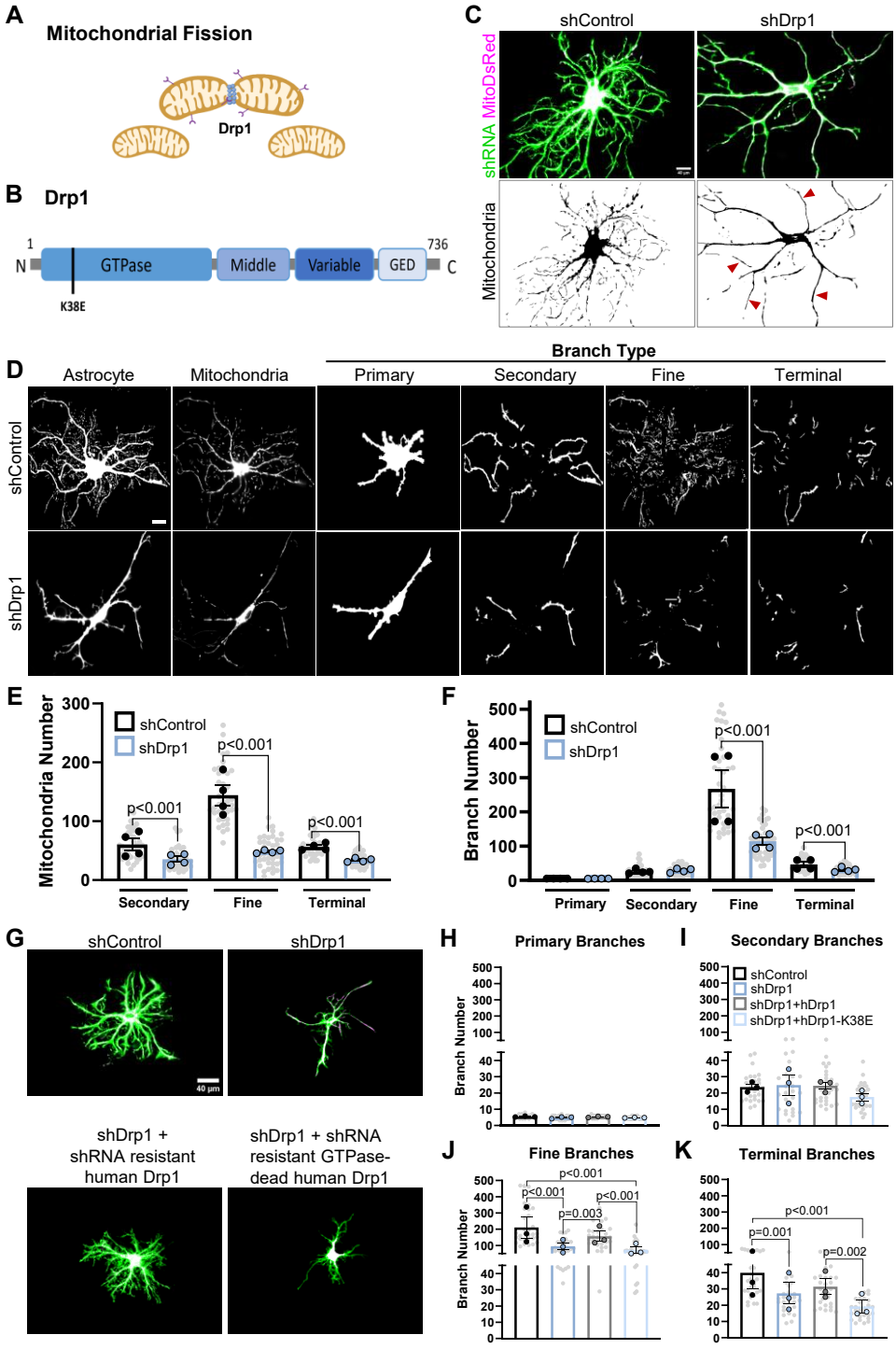

Supplemental 1: Validation of shRNA tools

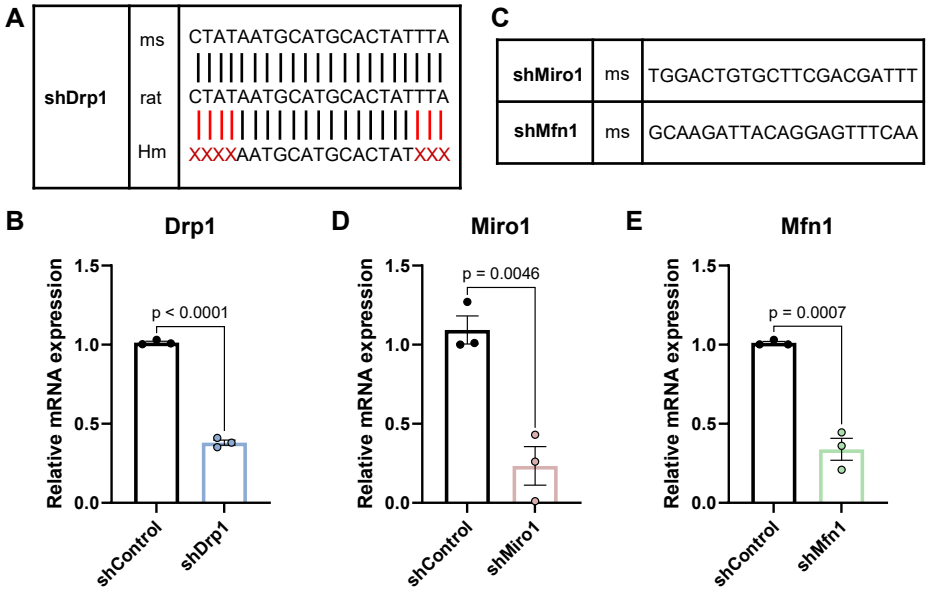

Fig 4: Mitochondrial fission, not fusion nor transport, is required for distal astrocyte process morphogenesis *in vivo*

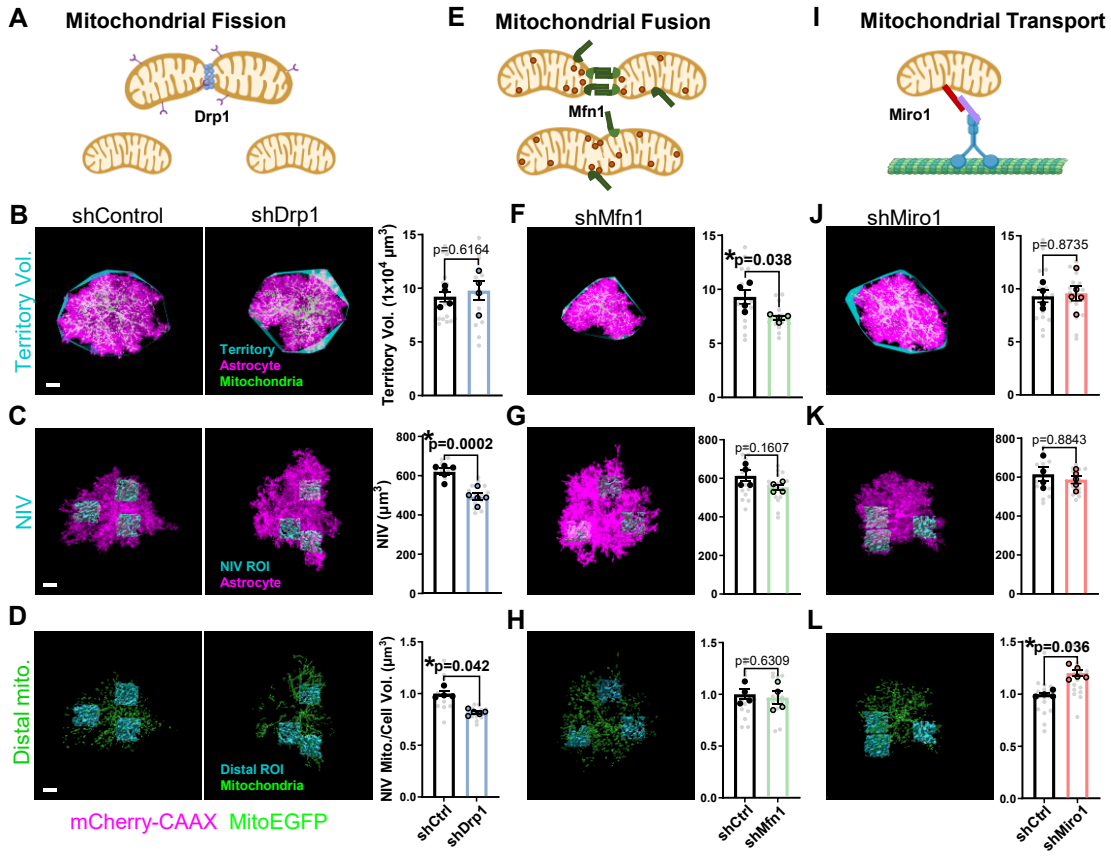

Supplemental 2: Genetic manipulation of mitochondrial dynamics in vivo alters mitochondria number and size

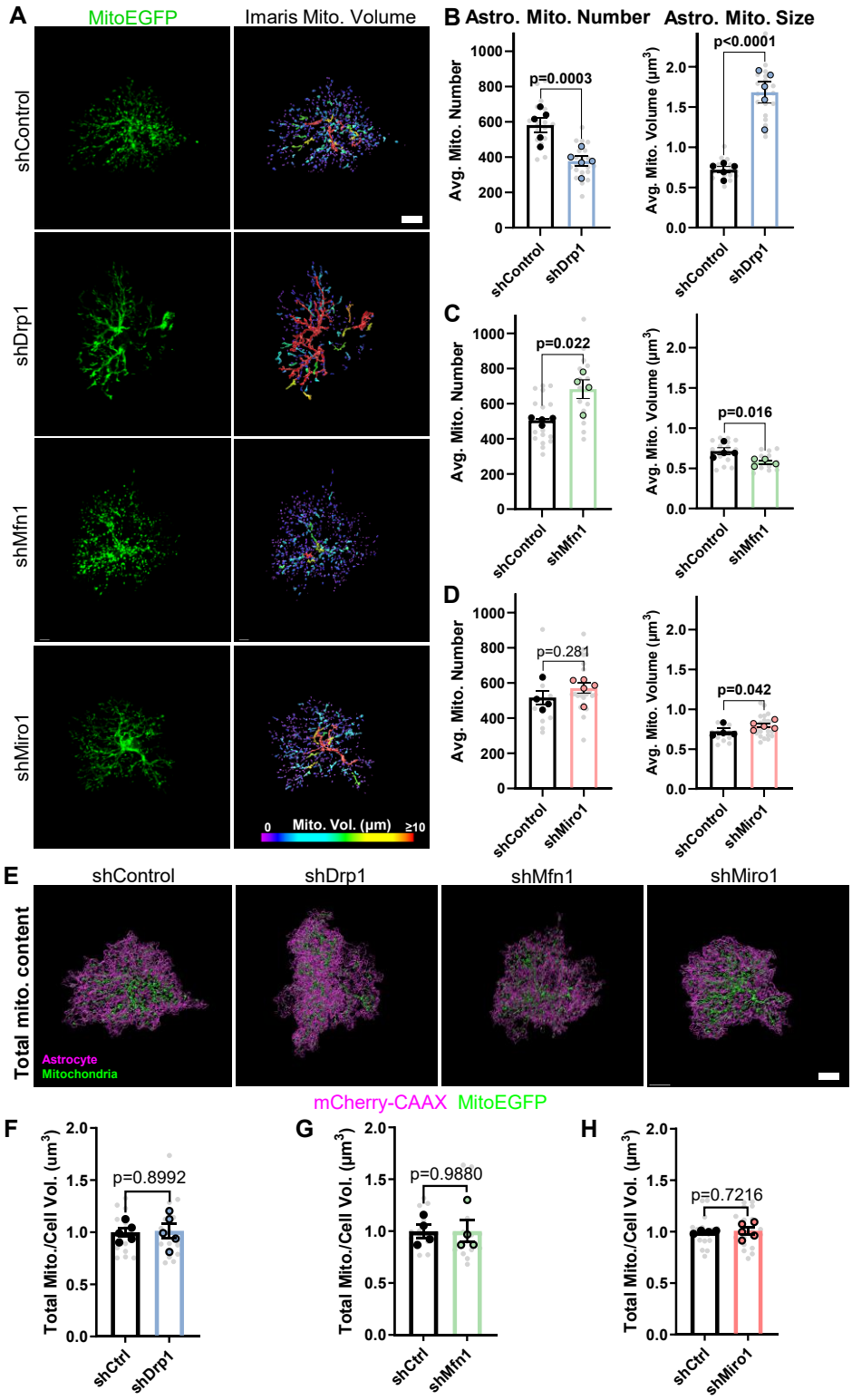

Fig 5: Drp1 controls cortical astrocyte organization during postnatal development

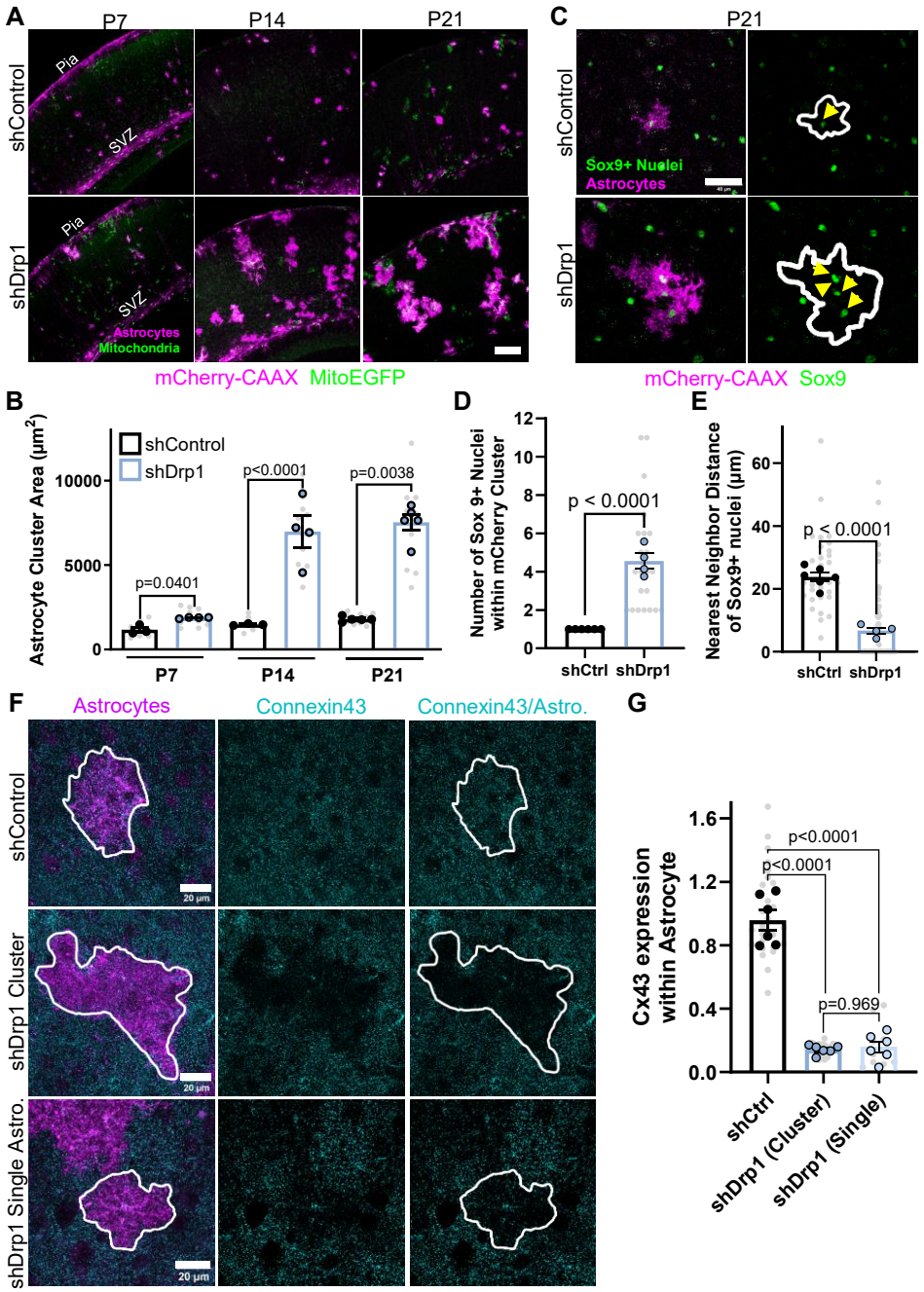

Supplemental 3: shDrp1-induced astrocyte clustering is not a result of increased astrocyte proliferation and is maintained through adulthood

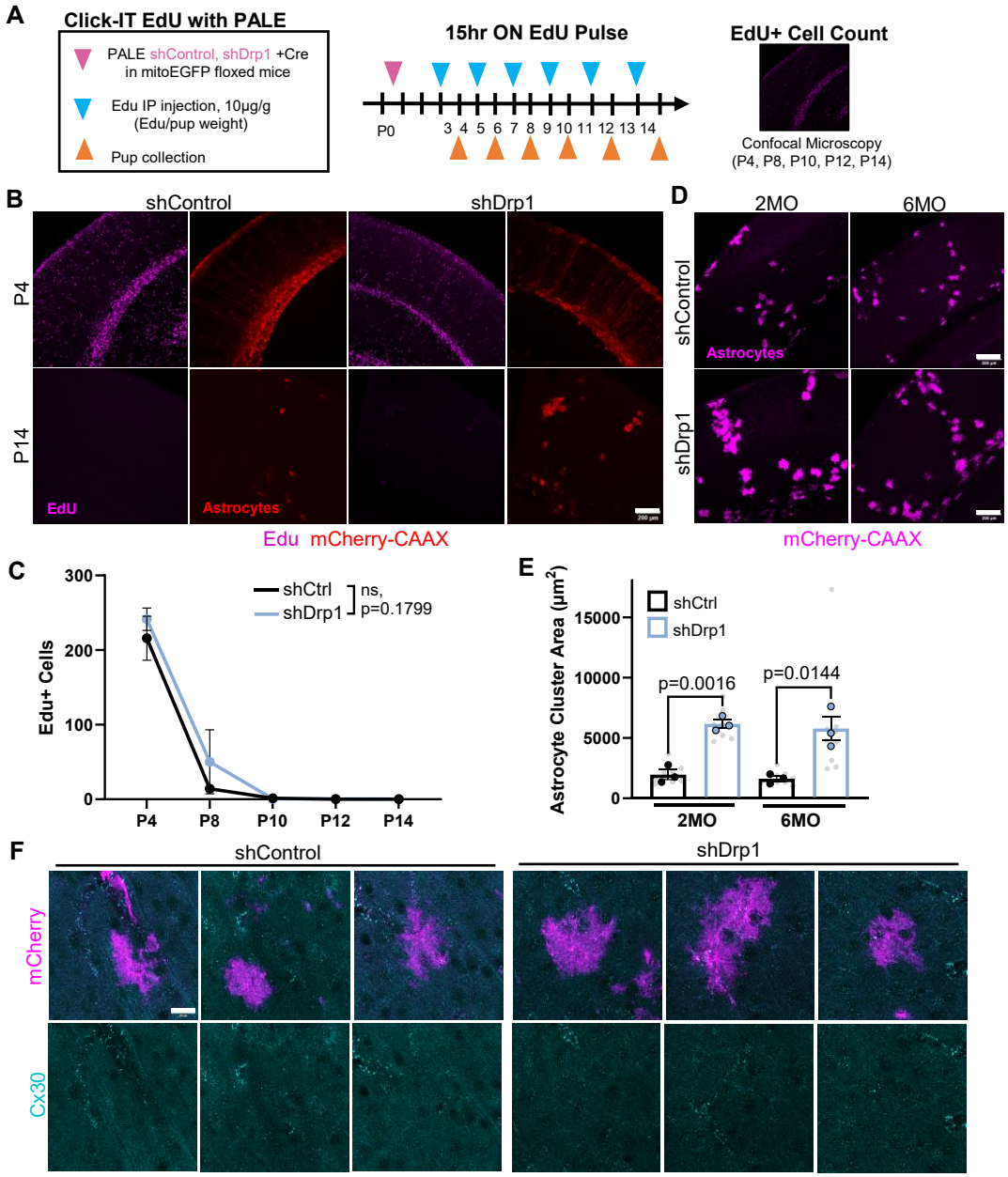

Fig 6: Astrocyte-specific Drp1 cKO induces cortical astrocyte reactivity

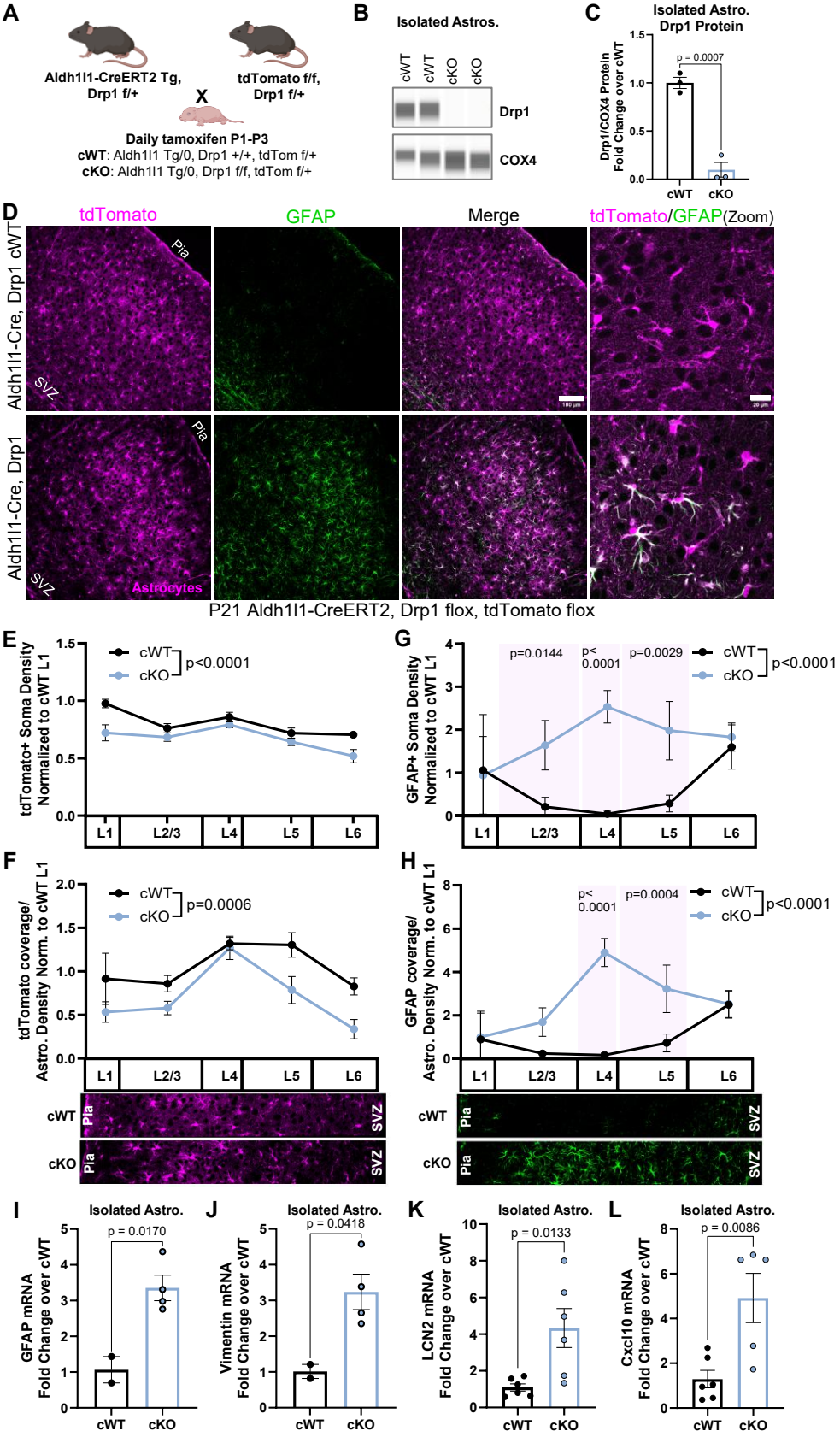

Supplemental 4: Astrocyte-Specific Drp1 cKO mouse characterization

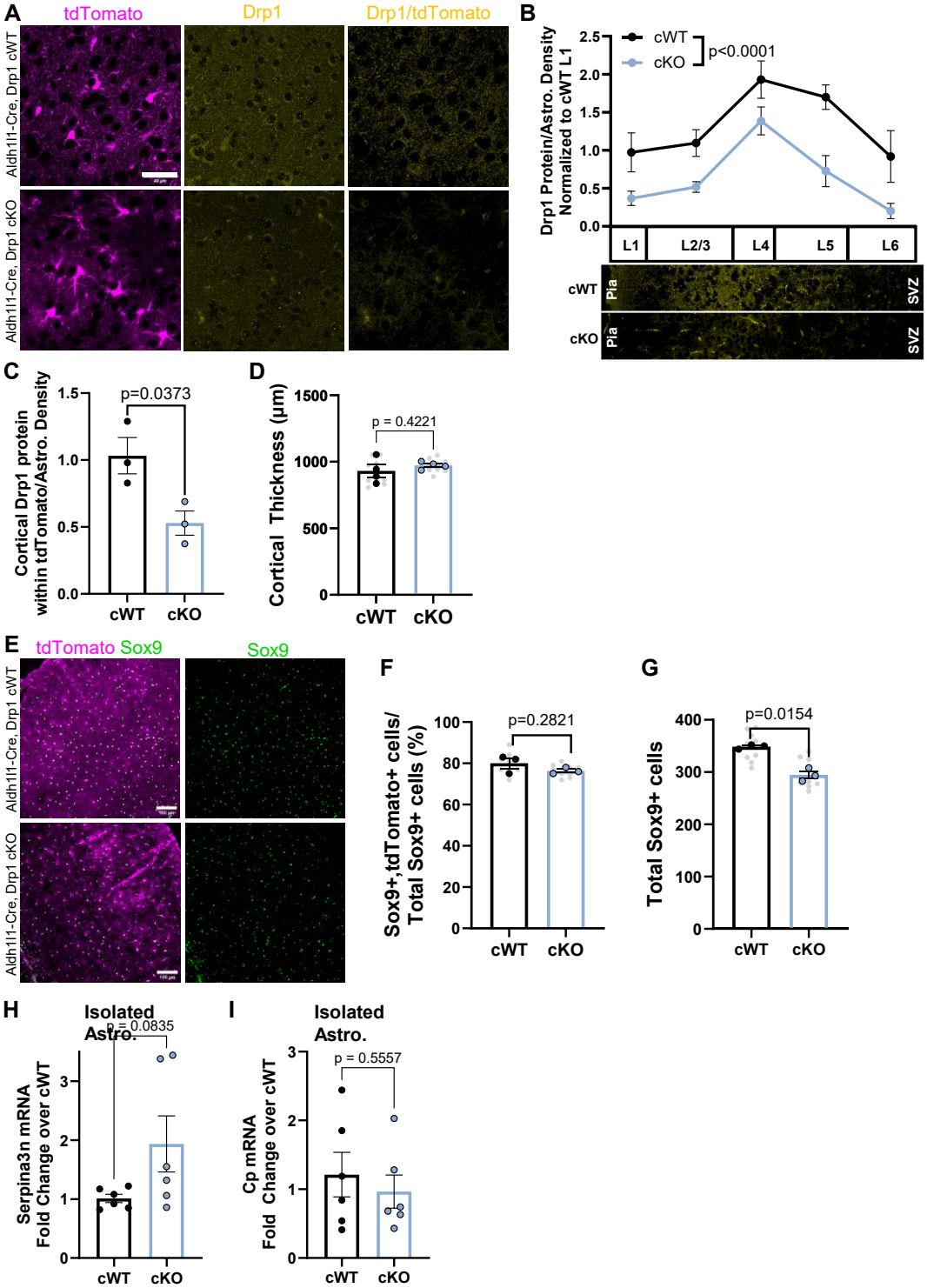
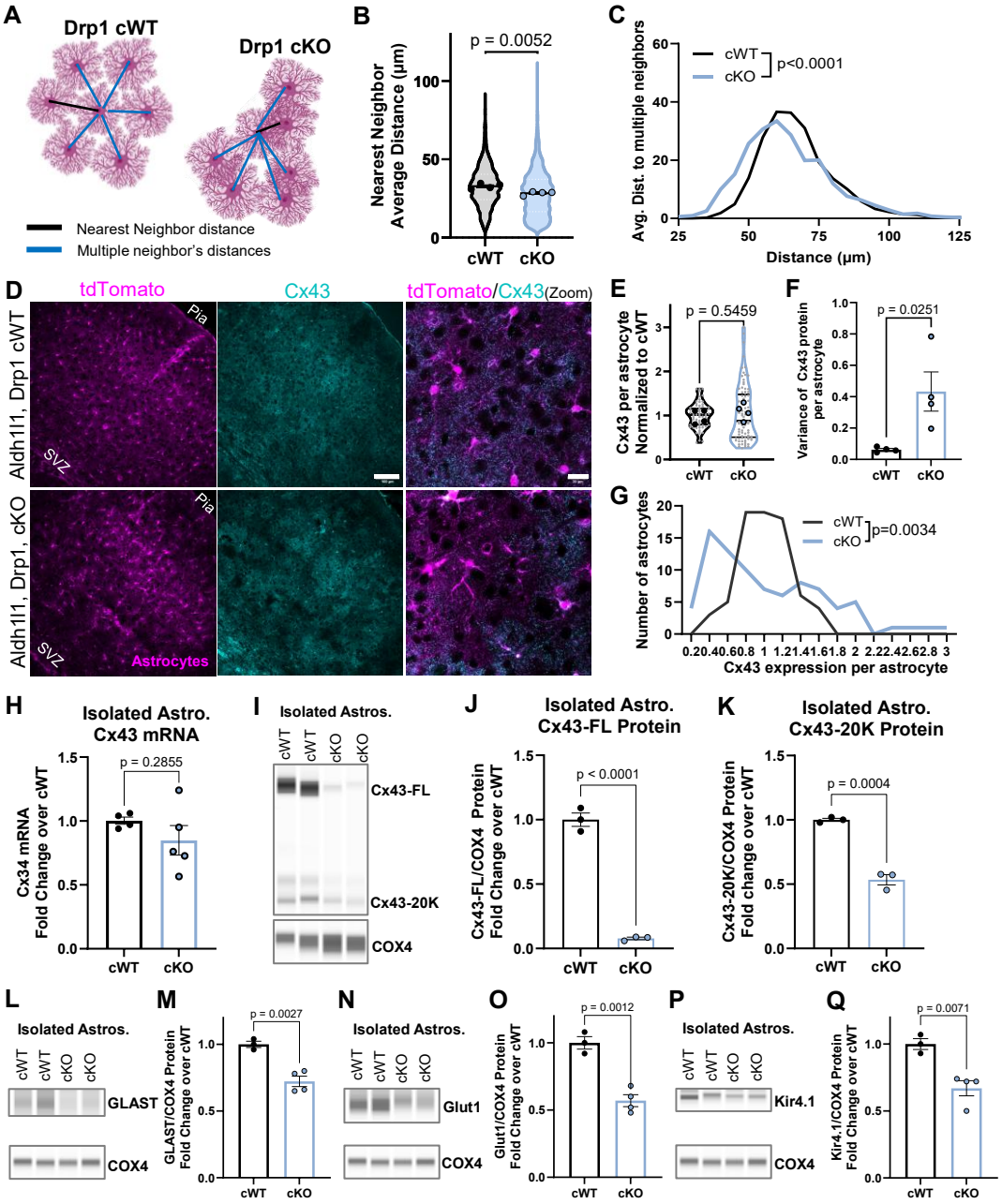
Fig 7: Astrocytic Drp1 loss dysregulates astrocyte organization and PAP protein expression in the mouse cortex